Relevance of symmetry for the synchronization of chaotic optical systems and the related Lang-Kobayashi model limitations

M. Matus, J. V. Moloney, and M. Kolesik
*Arizona Center for Mathematical Sciences, Department of Mathematics and Optical Sciences Center, University of Arizona, Tucson, Arizona 85721**

(Received 23 April 2002; published 22 January 2003)

Synchronization of chaotic semiconductor lasers has now been demonstrated experimentally in a variety of coupling schemes. Coupling methods include configurations where the transmitter laser system is itself chaotic and drives a receiver system, both lasers are individually chaotic, and both lasers induce the chaos through mutual coupling. The dynamics for each of these scenarios is in many cases adequately captured by the Lang-Kobayashi rate equation model. Such a simplified model, however, ignores fundamental aspects of the laser dynamics, such as the frequency and carrier density material susceptibility dependence, spatial hole burning effects, proper boundary conditions, and the fact that lasers may exhibit pronounced multilongitudinal dynamic behavior with and without the presence of a weak external feedback or injection. The model also cannot distinguish between many of the possible coupling geometries realizable in experiments. Using an interactive simulator based on the rigorous microscopic description of the light-matter interaction, we explore the unidirectionally coupled configuration, the relevance of symmetry for the synchronization achieved between two identical lasers, and the differences that arise when the traditional analysis through the Lang-Kobayashi model is compared to the full nonlinear partial differential equation model results.

DOI: 10.1103/PhysRevE.67.016208 PACS number(s): 05.45.Xt, 42.55.Px, 42.65.Sf

I. INTRODUCTION

The Lang-Kobayashi model [1] for a single-mode laser with a weak external feedback is the theoretical workhorse for computing and analyzing the behavior of chaotic lasers and their synchronization behavior. This model has proved very successful in capturing most of the qualitative behavior of both the chaos and the synchronization phenomena.

Chaotic dynamics in lasers with external feedback is now well established experimentally [2–5]. Synchronization of chaos between a master and slave lasers has also been observed by various groups worldwide [6–16], and there are reports on experimental works on chaotic communication system [17–19].

Chaos generation, synchronization, and their applications to communications are the topics extensively covered. Numerically and experimentally studied configurations include the ones where the transmitter system is a chaotic external cavity laser that drives a originally nonchaotic laser receiver [8,14,17,20–26], both the systems are chaotic external cavities and the receiver is unidirectionally coupled [9,12,13,16,18,19,26–35], and both systems induce the chaos through mutual coupling [36–40]. Similar coupling methods, but with different chaos generation mechanisms, have been also reported and analyzed [6,7,10,15,41–44].

In a numerical comparison of the three main coupling methods mentioned based on the Tang-Statz-deMars equations [45], it was suggested that the unidirectional coupling between two individually chaotic external cavity lasers is the best configuration for communication purposes, but some of the more robust synchronization experiments [12,14] have employed a diode external cavity laser as the master system and a near-identical laser as the slave one. In essence, this configuration is akin to an injection-locking experiment where the injected signal is chaotic rather than periodic.

Measurements have used a variety of detection methods. Typically, oscilloscope traces of relatively long-time power outputs over hundreds of nanoseconds tend to show excellent synchronization to the eye [8,12,13]. Slow time-scale synchronization tends to be a rather robust phenomenon and seems to occur without any special effort to ensure that the diode transmitter and receiver lasers are near identical (i.e., from the same wafer). The chaotic pulses observed on a picosecond time scale, resolved by short streak camera traces or fast photodiode sensors, had also shown good degrees of synchronization [14], but with the exception of power synchronization manifold reconstruction there appears to be no experimental measurements of the synchronization quality over the very long time intervals that practical chaos communication systems require.

The original Lang-Kobayashi (LK) model equation was derived using a simple isolated laser single-mode rate equation, augmented by a delayed field term associated to the external cavity feedback. The assumption is that the feedback is sufficiently weak, due to the very low reflectivity of the external feedback mirror (typically 1–5 %), so that multiple reflections in the external cavity can be ignored. Moreover, the LK model is a lumped system where all internal optical fields and carrier densities are averaged. The LK model cannot distinguish between individual members of a whole family of lasers whose mean reflectivity $R=\sqrt{R_1 R_2}$ is the same for different combinations of individual facet reflectivities. However, the internal distributed optical fields and carrier densities in the laser can be strongly nonuniform due to spatial hole burning or by the existence of internal asymmetries ($R_1 \neq R_2$, for example). To correctly resolve the entire system dynamics, it is necessary to use a full nonlinear

*URL: http://www.acms.arizona.edu

partial differential equation (FNPDE) model to describe the lasers with and without feedback.

We present results from a detailed study of the relevance of symmetry in the synchronization of chaotic semiconductor lasers, by using a FNPDE model integrated into an interactive simulation tool. The FNPDE model is built on the rigorous microscopic description of the light-matter interaction [46], and is solved via a highly efficient digital filter-based numerical algorithm for propagating light fields in complex, large-gain-bandwidth devices like semiconductor and fiber amplifier lasers [47]. It will be shown that complete or full synchronization is achievable when a symmetric system is employed, while when the symmetry is broken, different regimes of quality synchronization can be observed. The inherent limitations that arise in the Lang-Kobayashi model when asymmetric devices and systems are analyzed will also be shown.

II. THE OPTICAL SYSTEM SIMULATOR

The optical system simulator (OSS) tool employed here is an object-oriented approach to building a modular and flexible simulation environment capable of running interactively on a fast PC Unix work station, parallel machine, or in a distributed network environment. Prior to start-up, the user can set up an optical system that could consist of one or more semiconductor lasers or doped-fiber devices, attach gratings, HR/AR (high/antirefractive) coatings, external feedback reflectors, filters, etc. When running, different graphical interfaces can interrogate various components of the system and display internal optical and carrier density fields, detector averaged outputs, accumulated output spectra, eye diagrams, etc. The user can interactively modify certain device parameters on the fly, such as pump current, injection signal power, wavelength, current modulation frequency, and many others.

The simulator model used in this work is designed for systems in which the optical field is a single transverse mode. The field is represented by the projection onto the fundamental transverse mode, whose propagation is characterized by its phase index (or equivalently, propagation constant) and the group velocity v_g. At each point along the system's optical axis, the optical field is decomposed into forward and backward propagating components described by their complex amplitudes $\mathcal{E}^+$ and $\mathcal{E}^-$ that satisfy the partial differential equations

$$\partial_t \mathcal{E}^{\pm}(z,t) = \pm v_g \partial_z \mathcal{E}^{\pm}(z,t) \mp i\frac{\omega_R}{2}\int_0^{\infty} \chi[N(z,t),\tau]\mathcal{E}^{\pm}(z,t-\tau)\mathrm{d}\tau. \quad (1)$$

Here, ω_R stands for the reference frequency, and the convolution integral represents the locally changing susceptibility of the active layer. It may also include other optical properties of the cavity waveguide, such as the ''background'' loss. Both the gain and the refractive index change are calculated from a sophisticated many-body theory [46] and tabulated in terms of the frequency-dependent, complex susceptibility $\chi(N,\omega)$ that depends on the active-layer carrier

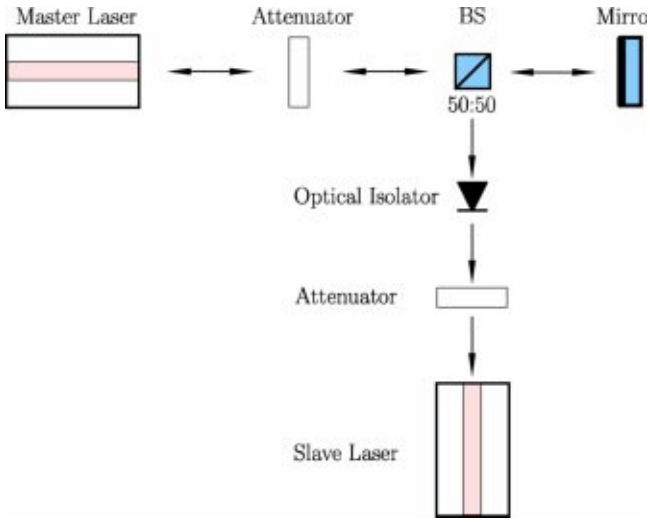

FIG. 1. The unidirectionally coupled system. On the horizontal axis a master device is driven into a chaotic regime by an external weak feedback. From the optical feedback path, an unidirectional injection is split off to the slave laser.

(sheet) density $N(z,t)$. The latter obeys an equation that includes the pump current density J, the density-dependent carrier recombination, and the interaction with the optical field,

$$\partial_t N = J/e - N/\tau(N) + \frac{A}{2\hbar}\mathrm{Im}\{\mathcal{P}\overline{\mathcal{E}}\}. \quad (2)$$

In the last term, $\mathcal{P}$ stands for the polarization and A represents the active-layer thickness. Similar to the optical field amplitudes $\mathcal{E}^{\pm}$, in our one-dimensional model the quantity $N(z,t)$ represents an amplitude of the transverse spatial profile of the carrier density distribution.

Numerical solution of these equations is not straightforward if the broad bandwidth and rich dynamics, inherent to some types of semiconductor lasers, have to be accurately captured. Our simulator engine is based on a spatial digital filtering of the evolving optical field to ensure that all spectral components propagate with the correct gain/loss and phase velocity given by the local susceptibility $\chi(N(z,t),\omega)$. The reader is referred to Ref. [47] for details. The structure of the simulator is modular, allowing to ''build'' the simulated system from modules such as the active-laser cavity (described by the above equations), passive ''cavities'' for free-space propagation, laser facets, and various optical interfaces.

III. THE UNIDIRECTIONALLY COUPLED SYSTEM

In order to analyze the relevance of symmetry in the synchronization of unidirectionally coupled lasers, we studied the system shown in Fig. 1, where on the horizontal axis a master laser is driven into a chaotic regime by a weak external feedback. An identical slave laser is also driven into a chaotic regime by the unidirectional external injection split off from the master laser feedback path.

Figure 2 shows an equivalent system where a synthetic interface between the lasers sends a weak feedback into the

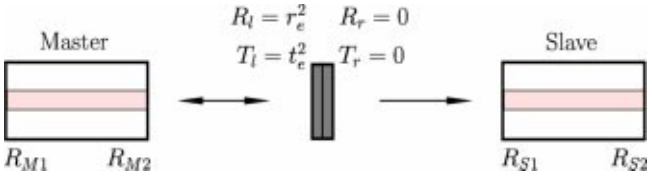

FIG. 2. Equivalent unidirectionally coupled system. The reflection coefficient r_e produces the master feedback, and the transmission coefficient t_e produces the unidirectional slave injection. This is a truly equivalent model of the system shown in Fig. 1.

master laser and an unidirectional injection to the slave. The synthetic interface, defined with different left and right reflectivities and transmittivities, allows multiple reflections in the external master cavity but prevents any slave signal from going back to the master or to the slave itself. This synthetic interface provides a truly equivalent system and not an approximation to the original system in Fig. 1. The master and slave facets that receive the feedback and the injection are called the *perturbed facets*.

Figure 3 shows a symmetric unidirectionally coupled system, where both attenuation coefficients r_e and t_e are equal, both lasers are identical, and they are oriented in such a way that the lasers face the feedback or unidirectional injection through equivalent facets. When the system is symmetric, both lasers experience the same perturbation E_p.

Starting from the symmetric case, and by flipping the orientation of the lasers, up to four possible configurations can be realized, as is shown in the example in Fig. 4. In general, two of the four resulting cases are no longer symmetric. Of course, in the particular case where the lasers are symmetric by themselves and their facet reflectivities are equal ($R_1 = R_2$), there will be only a single symmetric configuration.

In this study it is also implicit that the external cavities have equal lengths and their round trip times are both equal to τ. However, if the cavity lengths are different, it is just a matter of time shifting the slave output by the difference between the master external cavity round trip time τ and the laser time separation τ_c, before any further analysis, and the same dynamics will be observed.

The LK model, by lumping the laser systems into scalar equations, cannot always distinguish between each of these four configurations. Yet, from an experimental point of view, the relative orientation of the HR/AR coated facet lasers should be expected to influence the synchronization quality. For reference purposes, the LK model for the unidirectionally coupled system shown in Fig. 2 is reproduced in Eqs.

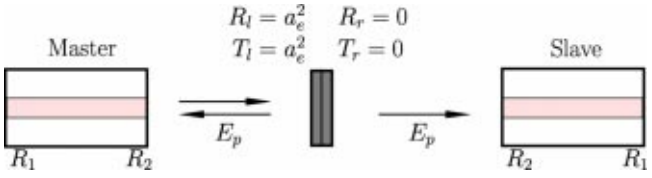

FIG. 3. A symmetric unidirectionally coupled system. Here the feedback and injection strengths are equal, both lasers are identical, and they face the feedback/injection through the equivalent facets with the same reflectivity R_2.

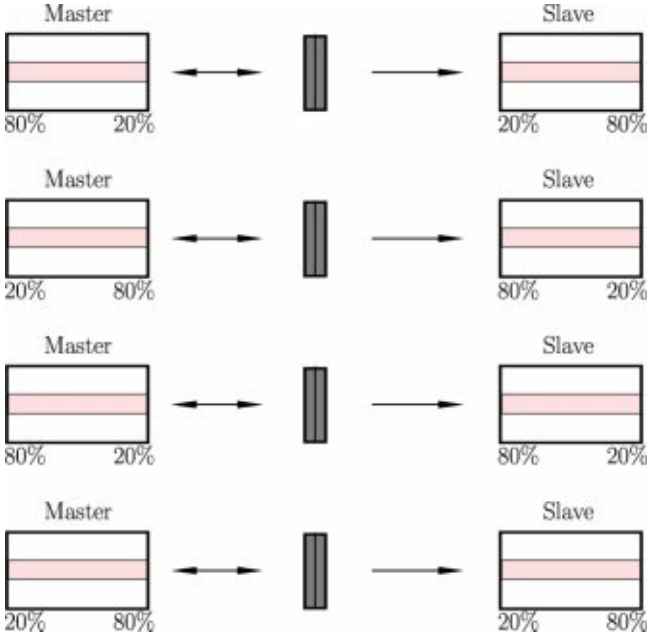

FIG. 4. Possible configurations of two identical HR/AR lasers in the unidirectionally coupled system. In the two top ones (80:20⇔20:80 and 20:80⇔80:20), the resulting system is symmetric, in the two bottom ones (80:20⇔80:20 and 20:80⇔20:80) the symmetry is broken.

(3), where variables and parameters have the standard meaning found in the literature (see Table I)

$$\frac{dE_m(t)}{dt} = \frac{1+i\alpha}{2}\left[G(N,E_m^2) - \frac{1}{\tau_p}\right]E_m(t) + \frac{\kappa_m}{\tau_{in}}E_m(t-\tau)e^{-iw_0\tau},$$

$$\frac{dE_s(t)}{dt} = \frac{1+i\alpha}{2}\left[G(N,E_s^2) - \frac{1}{\tau_p}\right]E_s(t) + \frac{\kappa_s}{\tau_{in}}E_m(t-\tau)e^{-iw_0\tau}, \tag{3}$$

$$\frac{dN_m(t)}{dt} = J - \frac{N_m(t)}{\tau_s} - G(N,E_m^2)E_m(t)^2,$$

$$\frac{dN_s(t)}{dt} = J - \frac{N_s(t)}{\tau_s} - G(N,E_s^2)E_s(t)^2,$$

$$G(N,E^2) = G_n(N-N_0)(1-\epsilon E^2).$$

The LK model reduces the laser reflectivities R_{i1} and R_{i2} to a mean reflectivity $R_i = \sqrt{R_{i1}R_{i2}}$, which enters the LK model through the photon lifetime parameter τ_p, and the internal fields and carrier densities are lumped into the scalar values E_i and N_i. The model assumes that the lasers are single mode, and that multiple reflections in the external cavities can be neglected. In fact, there is a much stronger assumption that reduces its applicability range: the LK model requires that the coupling coefficients κ_m and κ_s, defined [1,48] as

TABLE I. Meaning of the variables and parameters in the Lang-Kobayashi model equations (3).

$E_{m,s}(t)$	Master and slave optical fields
$N_{m,s}(t)$	Master and slave carrier populations
G_n	Modal gain coefficient
N_0	Carrier density at transparency
ϵ	Nonlinear gain coefficient
τ_p	Photon lifetime
τ_s	Carrier lifetime
α	Linewidth enhancement factor
J	Injected current density
τ	Round trip time for the external cavity
τ_{in}	Round trip time for the internal laser cavity
κ_m	Feedback coupling factor
κ_s	Injection coupling factor

$$\kappa_m = r_e \frac{1-R_{M2}}{\sqrt{R_{M2}}} \equiv r_e \frac{t_m^2}{r_m},$$

$$\kappa_s = t_e \frac{\sqrt{1-R_{M2}}\sqrt{1-R_{S1}}}{\sqrt{R_{S1}}} \equiv t_e \frac{t_m t_s}{r_s}, \tag{4}$$

have to be significantly smaller than 1. This is equivalent to require that the external feedback strength r_e^2 or injection strength t_e^2 must be absolutely and relatively smaller than the perturbed facet reflectivities r_m and r_s, respectively. This is a restriction very hard to satisfy for highly effective HR/AR coatings, as for example in a 95:1% configuration, unless extremely weak feedback and injection strengths are employed.

In the LK model, the only parameters that depend on the orientation of the lasers are the coupling coefficients κ_m and κ_s. From Eq. (4), it is easy to see that there exists a whole family of master-slave configurations, which appears identical within the LK model. Namely, if we define a global LK coupling coefficient κ and constrain the feedback strength r_e and injection strength t_e such that

$$r_e = \kappa \frac{r_m}{t_m^2}, \quad t_e = r_e \frac{r_s}{r_m}\frac{t_m}{t_s}, \tag{5}$$

then the LK equations (3) will be the same for any choice of the master/slave facet reflectivities/transmittivities.

Once the external r_e and t_e coefficients are adjusted, like in Eq. (5), the internal coupling coefficients κ_s and κ_m will be equal for all the cases, and from the simulation and analysis point of view under the LK model, all the configurations in Fig. 4, symmetric or not, must yield equivalent solutions and equal degrees of synchronization. However, when the FNPDE model is used and the laser orientations are taken into full account, very different dynamics and degrees of synchronization are observed for the symmetric and asymmetric cases, even when an unique global LK coupling coefficient is employed in all the configurations. In order to see how much of physics is lost in the LK picture, we concentrate on the ''LK-invariant'' family derived from the example in Fig. 4 and compare the predicted invariability against the results of the FNPDE model. But before going into more specific descriptions of the results, we will introduce a local synchronization measure by defining the *synchronization index*. We will also introduce the averaging method used to mimic different experimental measurement techniques.

IV. THE SYNCHRONIZATION INDEX

When we say that two systems are synchronized, we mean that they are in some way coupled and their dynamics are almost identical. In a master-slave system, where the coupling occurs unidirectionally from the master system to the slave, this means that the slave must reproduce the master's dynamics closely.

In general terms, if $\vec{x}$ is the master state variable vector, $\vec{y}$ the slave state variable vector, C the coupling operator from the master to slave, and S a similarity relation, then we say that the systems are synchronized if the distance between the system trajectories is always smaller than a given tolerance ε,

$$\langle \vec{y}(C(\vec{x}(t)),t), S(\vec{x}(t-\Gamma)) \rangle \leqslant \varepsilon, \tag{6}$$

where $\langle , \rangle$ is a distance metric and Γ a delay (positive) or anticipation (negative) time shifting constant. Usually, the distance operator does not involve the entire state vectors but some scalar observed variables $x(t)=O_m(\vec{x}(t))$ and $y(t)=O_s(\vec{y}(t))$, where O_m and O_s are some observing projections. If the observed variables are output power signals (positive quantities), then the similarity relation that ensures near identity in the time and spectral domains is a simple scaling relation. Thus, in the ideal case where the distance between the observed variables is zero, the following relation must hold:

$$y(t) = b x(t-\Gamma), \tag{7}$$

where b is a positive constant scaling factor. The criterion does not include an additive term, because if we use $y(t)=a+bx(t-\Gamma)$ instead, the constant a introduces an arbitrary frequency peak at the zero or reference frequency, destroying the similarity between the transmitter and receiver spectra.

Therefore, to locally quantify the synchronization between two discrete power signal samples $\{x_i\}$ and $\{y_i\}$ that are properly in phase (i.e., after time shifting one of the signals by any required time shift Γ), we probe the scaling relation by first obtaining the best scaling factor b, using the standard least-squares approach

$$b = \frac{\sigma_{xy}}{\sigma_{xx}}, \quad \sigma_{xy} = \sum_i^N x_i y_i, \tag{8}$$

where N defines the total sample length or a significant part of it. Next we compute the *synchronization index* (SI), denoted as S_i, for every sample pair defined as

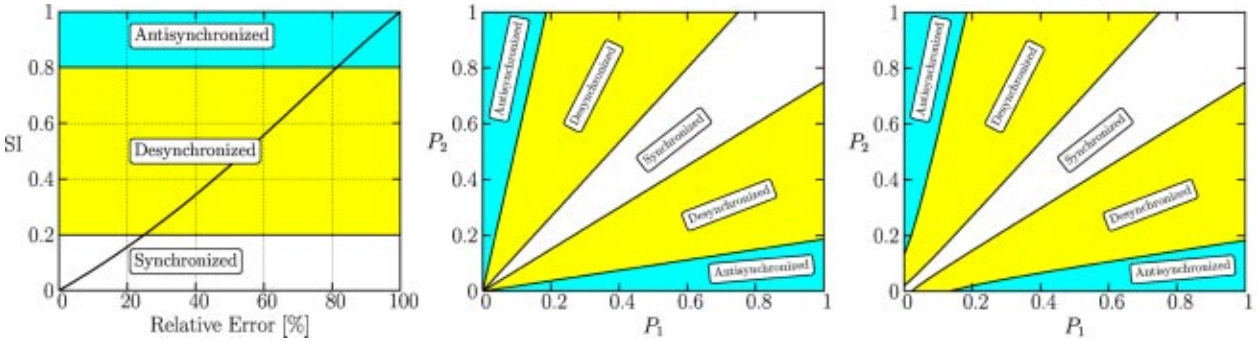

FIG. 5. The synchronization index (SI) and its relation to the relative error and the power synchronization manifold (PSM). The left picture shows the SI in terms of the relative error between the two normalized power signals and the synchronization intervals. The middle picture shows the PSM diagram with the different synchronization regions. The right picture shows how these regions open up around the origin when a threshold value of 0.1 is added as in Eq. (10).

$$S_i = \sqrt{\frac{(y_i - bx_i)^2}{y_i^2 + b^2 x_i^2}}. \tag{9}$$

The synchronization index S_i locally measures the relative distance between $\{y_i\}$ and the "prediction" $\{bx_i\}$. Since the power samples x_i and y_i are positive, the synchronization index will be near or equal to 0 when the signal values are similar ($y_i \approx bx_i$), and close or equal to 1 when they are opposites, i.e., in the extreme case when y_i is much bigger than bx_i, or vice versa (consider, for example, the situation where $x_i = 0$ and $y_i = 1$).

Figure 5 (left) shows how the synchronization index behaves in terms of the relative error between two normalized power values. As the relative error between the two signals increases, the synchronization index goes from 0 to 1 almost linearly. With this in mind, we will say that the two signals are locally *synchronized* when the SI values are in an interval close to 0 (the power values are very close to each other), *antisynchronized* when the SI values are in an interval close to 1 (the power values are opposite ones), and *desynchronized* when the SI values are neither close to 0 nor to 1.

The exact boundaries of the synchronization intervals are arbitrary, but once they are chosen, corresponding power synchronization manifold regions can be associated with them through Eq. (9), as is shown in Fig. 5 (middle). For the present analysis, we defined the synchronized interval for SI values smaller than or equal to 0.2 (relative error smaller than 25%) and the antisynchronized interval for SI values greater than or equal to 0.8 (relative error greater than 82%). The desynchronized interval is therefore defined for SI values between 0.2 and 0.8. In a real system the interval choice could be related, for example, to some detector characteristic.

In systems where the output powers are allowed to reach levels close to the numerical or physical noise, it is desirable to assume that two power values at the noise level are always similar, independent of their actual values [consider, for example, the case where $bx_i = 10^{-4}$ mW and $y_i = 10^{-6}$ mW, which in Eq. (9) produces $S_i \approx 0.99$, but it is specified that values smaller than 10^{-2} mW are noise]. To include this criterion, the synchronization index is corrected by adding a threshold value as follows:

$$S_i = \sqrt{\frac{(y_i - bx_i)^2}{y_i^2 + b^2 x_i^2 + U^2}}. \tag{10}$$

With this correction, whenever y_i and bx_i are much smaller than the threshold U, the synchronization index will always be small. Figure 5 (right) shows the effect of adding the threshold on the power synchronization manifold regions. It can be seen that the synchronization regions open up around the origin, allowing one to include different small noise power values in the synchronized region [now $bx_i = 10^{-4}$ mW, $y_i = 10^{-6}$ mW, $U = 10^{-2}$ mW and Eq. (10) produce $S_i \approx 0.01$].

V. OBSERVATIONAL TIME SCALES AND DETECTOR RESPONSES

In order to capture the differences between the experimental observations using different means of detection or detector responses, we need to introduce the notion of the observational time scale. But first, we must remark that the time step Δt used in our simulations is of the order of 100 fs. Therefore, we can access or observe the laser output at a time scale much finer than that achievable in experiments. To mimic experimental observational time scales, we preprocess the simulation output data by applying an exponential average filter using different response times. Thus, if $\{x_i^s\}$ is our raw simulation data output, then the data used for synchronization analysis $\{x_i\}$ are obtained through the iterative formula

$$x_i = (1-\lambda)x_{i-1} + \lambda x_i^s, \quad x_0 = 0, \tag{11}$$

where $\lambda \in (0,1]$ is the parameter that defines the response time of the filter. To understand the role of λ, we rewrite iterative expression (11) like the equivalent exponential average,

$$x_i = \sum_{j=0}^{i-1} w_j x_{i-j}^s, \quad w_j = \lambda(1-\lambda)^j, \quad \sum_{j=0}^{\infty} w_j = 1. \tag{12}$$

When λ is close to 1, the filtered value will be mainly defined by the most recent sample data, since the individual

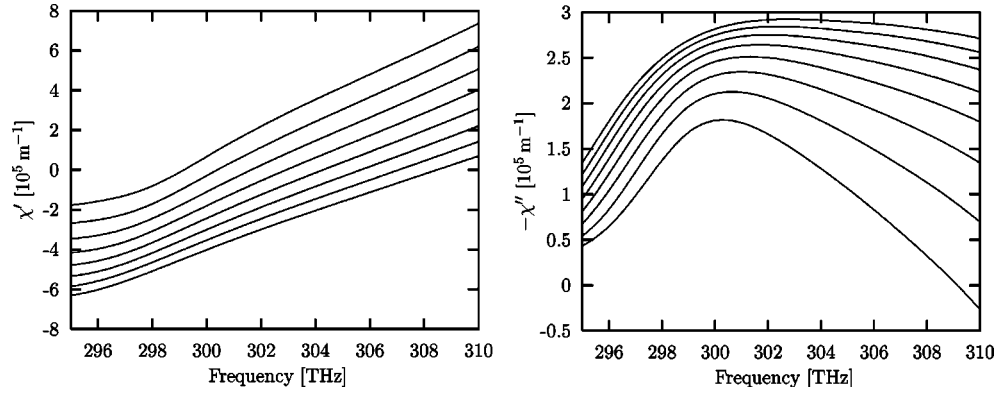

FIG. 6. Material susceptibility curves for different carrier densities in the relevant frequency range. The χ' picture shows the real part curves, starting from the top, for equally spaced carrier density values in the range from 2.5×10^{16} m^{-2} to 6×10^{16} m^{-2}. The $-\chi''$ picture shows the negative imaginary part (gain) curves, starting from the bottom, for the same carrier density values.

weights w_i tend to zero exponentially. If λ is decreased, the past sample data will become more important as the weights decay slower. To get an idea of how much the past sample data contributes to the filtered output, we define the filter response time (FRT), denoted as F_{RT}, as the time window that involves 95% of the accumulated weights, i.e.,

$$\mathrm{F_{RT}}(\lambda)=N_\lambda \Delta t, \quad \sum_{j=0}^{N_\lambda} w_j = 95\%. \tag{13}$$

By using different filter response times, or λ values, we can choose different observational time scales, mimicking what is observed by different detection devices. The slowest time scale resolution would correspond to oscilloscope traces (FRT of the order of nanoseconds), the fast ones to streak camera traces (FRT of the order of picoseconds), and the fastest ones to ''ideal instrument'' traces (FRT of the order of femtoseconds or less). A similar but simpler distinction has been used in Ref. [21] with the names of *macroscopic* and *microscopic* time scales.

VI. RESULTS

To understand the relevance of the symmetry on the system synchronization, we simulated the four configurations shown in Fig. 4 for two identical asymmetric 80:20% HR/AR coated devices, trying to keep everything the same, except for the laser orientations. The laser models were Fabry-Perot cavities, 250 μm long with an active-layer build of a 10-*nm* $In_{0.2}Ga_{0.8}$ well with $Al_xGa_{(1-x)}As$ barriers, where x rises linearly with the distance from the well from 0.1 to 0.6 over 85 nm. Figure 6 shows the resulting susceptibility values χ for the active-layer composition and its frequency and carrier density dependence. The χ values are fed into the OSS simulator through look-up tables for efficient computation.

The lasers were operated just above the solitary threshold current where they lase on a single mode at a frequency of 302.995 THz. The external cavities were 30 cm long. The one attached to the master laser allows multiple reflections. The output field observations were made at the perturbed facet, over 1 μs of simulation time using a $\Delta t=125$ fs time step. The output field data was recorded every 250 fs, enough to cover the relevant output bandwidth, and the initial 50 ns transient time was discarded.

Starting with the 80:20⇔20:80 case, the feedback r_e^2 and injection t_e^2 strengths were set to 0.2%. In this initial regime, the system shows very rich dynamics. Figure 7 shows very asymmetric internal forward and backward fields profiles, greatly influenced by the HR/AR coatings and the multimode regime. The resulting internal carrier density profile, also asymmetric, is a clear evidence of strong spatial hole burning.

The pictures in Fig. 7 are placed in the same way as the lasers face each other in the simulated configuration. Therefore, the right value of the master forward field profile enters like an attenuated injection at the left side of the slave forward field profile. The configuration and the highly synchronized regime make the plots look like mirror images, where the slave backward/forward field profile is a mirror image of the master forward/backward one.

The same mirror image effect is visible in the carrier density profiles, showing that the lasers are synchronized not only with respect to the observed power output values, but in the entire state variable space. Note that while the in the LK model a laser is realized with only $2E+1N=3$ state variables, within the FNPDE model each laser equation system has $(4E+1N)\times N_g-1$, where N_g is the number of grid points. In particular, for the laser lengths and the time step used, N_g is 31, resulting in 154 state variables for each laser. The multidimensional FNPDE model is therefore weakly coupled, since it has 154 state variables coupled through two injected field variables (compared to the LK model that has only three state variables coupled through two injected field variables), but still is strongly synchronized.

As can be seen in Fig. 7 (middle), the external weak feedback not only produces a multimode regime, but it also shifts the laser output frequency by about 0.75 THz from the isolated 302.995-THz lasing mode. The resulting spectra spread over nearly 1.5 THz, showing around ten longitudinal modes. The zooming into one of the laser modes displayed in Fig. 7 (bottom) also shows that the individual modes are broadened considerably, and the external cavity modes are

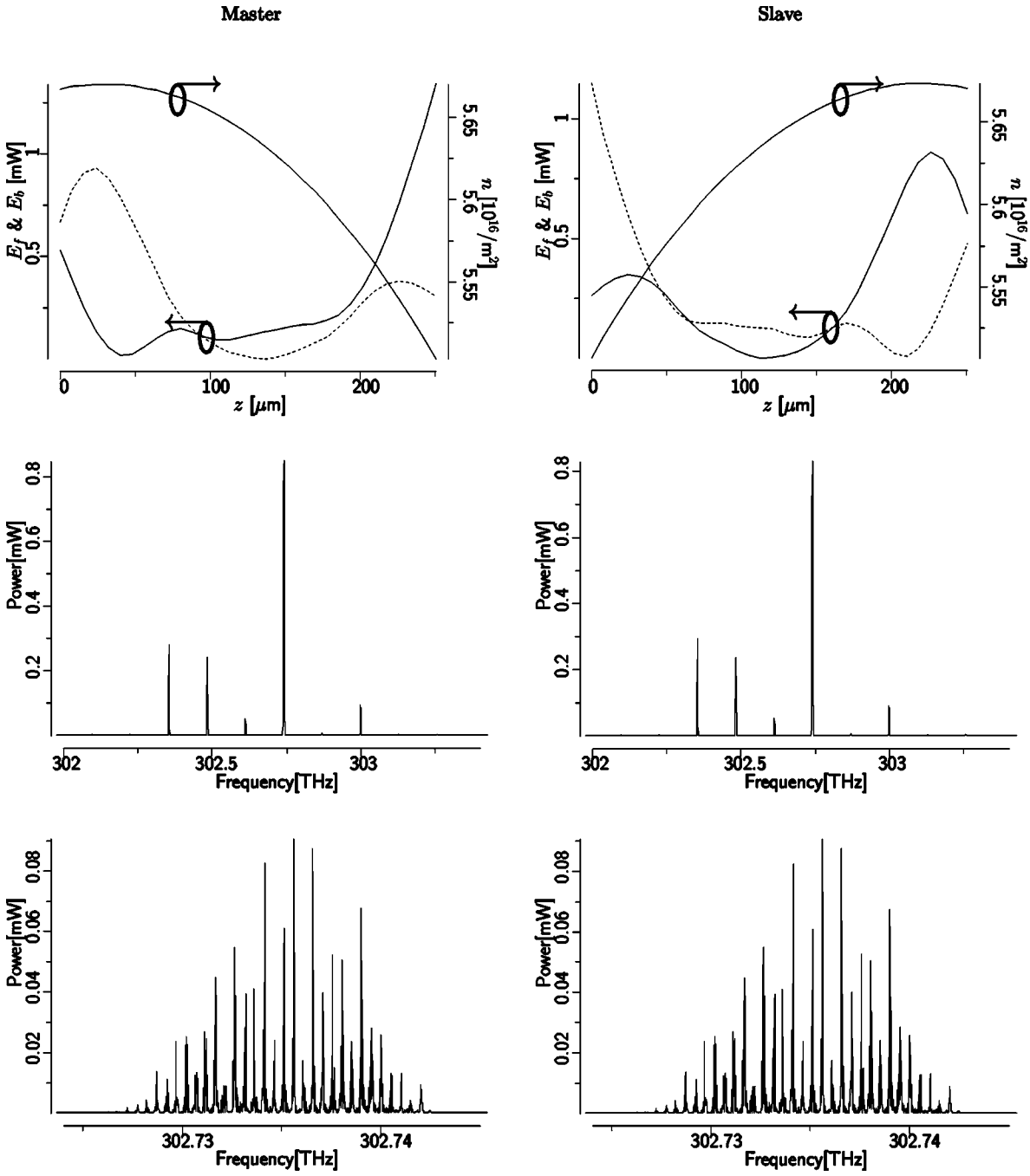

FIG. 7. Snapshot of the dynamic observed in the 80:20⇔20:80 symmetric case. The top pictures show the internal fields (solid line for the forward field and dashed for the backward field) and carrier density profiles. The middle pictures show the multimode regime and the bottom ones show the broad chaotic signature in one of the frequency modes.

clearly visible as the regularly spaced peaks. The spectra, just like the internal profiles, look identical at both frequency resolutions because the optical field outputs were very well synchronized in amplitude and phase. Also note that the spectra pictures are ''single shots'' at a given time, and the signal spectra is not static. They change dynamically, exhibiting chaotic mode power transfer and beating during the entire simulation as the antiphase dynamics observed experimentally in Ref. [16].

We then proceeded to compare the different power and SI time series for different observational time scales of 7.5 ns, 750 ps, and 75 ps, corresponding to λ values of 10^{-4}, 10^{-3}, and 10^{-2}. For easier visualization, the slave power time series were scaled by using the b factor computed according to Eq. (8).

Figure 8 shows the results for the symmetric 80:20⇔20:80 case. As observed before, the synchronization quality is very high, where the SI values for the slowest time scales are always smaller than 0.01, where the greatest values occur during the power dropout event, and no visible difference between the power time series can be observed. For the faster time scales, the SI spike values increase, but

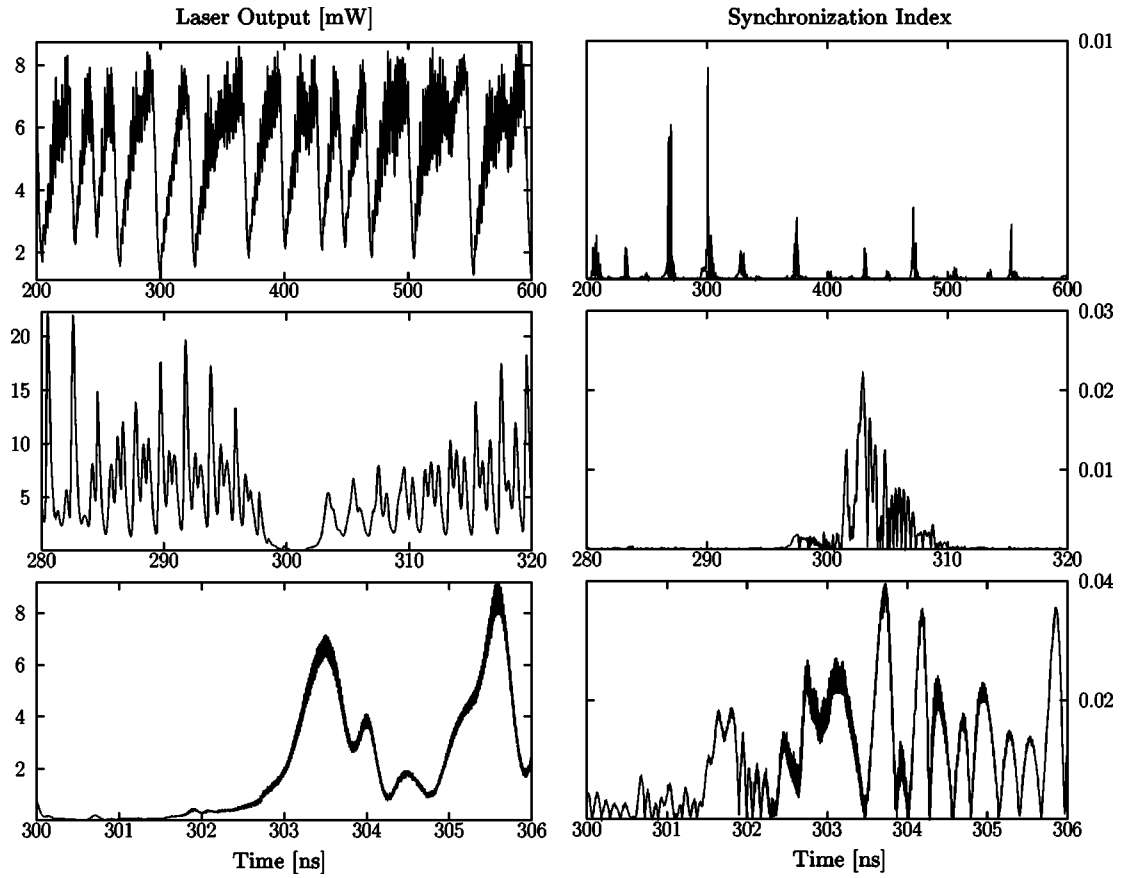

FIG. 8. Power (master and slave lines not distinguishable) and synchronization index time series for the 80:20⇔20:80 case (see Fig. 4) at different time scales (starting from the top, filter or ''detector'' response times of 7.5 ns, 750 ps, and 75 ps).

not enough to show visible difference between the signal even at the fastest time scales. The origin of the high similarity between the signal outputs, independent of the time scale employed, is the complete or full synchronization achieved in this configuration, which extends to the entire state variable space.

As we said before, to study the relevance of symmetry, we tried to keep the system the same for the four possible configurations, except for the laser orientations. Hence, in the three remaining cases we first adjusted the external feedback strength r_e^2 and injection strength t_e^2 according to Eq. (5), maintaining the same global LK coupling coefficient used in the first case. In this way, we will cancel the effects of changing the external coupling coefficients κ_m and κ_s when we flip the lasers, and we could analyze the effects of the remaining internal laser asymmetries.

Thus, for the symmetric case 20:80⇔80:20, the global LK coupling coefficient was maintained by making both the feedback strength r_e^2 and injection strength t_e^2 equal to 3.2%. Figure 9 shows, like the previous symmetric case, that both laser outputs look identical on the slowest time scales, and only some small differences can be observed on the fastest ones during some of the power dropout recovery events. The slight loss of synchronization is due to the statistical independence of the laser noise sources and due to the weaker synchronization characteristic of this configuration.

The synchronization observed in these symmetric cases has been previously called complete or full synchronization [10,12,24,39], referring to the mathematical sense where both the master and slave systems yield near or identical solutions. Complete synchronization has been observed in numerical simulations based on the LK model where two identical devices are considered, but there are no experimental reports about it, since it seems to be very sensitive to the parameter mismatch [22]. Therefore, it is interesting to observe that the FNPDE model, which is highly multimode and multidimensional (as is a real system), also shows this kind of synchronization.

In the asymmetric case 80:20⇔80:20, the feedback strength r_e^2 and injection strength t_e^2 were adjusted to 0.2% and 3.2%, maintaining the same LK coupling coefficient as before. Figure 10 shows the resulting power and SI time series, where it can be observed that in spite of the coupling coefficient adjustments, the synchronization quality is not comparable to the previous symmetric cases. Particularly interesting is the fact that the slave power time series shows a kind of laggard behavior when the slave power dropouts are consistently shifted with respect to the master ones, producing the corresponding high spikes in the SI graphs.

The lag synchronized regimes have been also found numerically using the LK model [10,22–24,27] and experimentally in Refs. [12,14]. In most of these cases the slave injection was stronger than the master feedback, making it

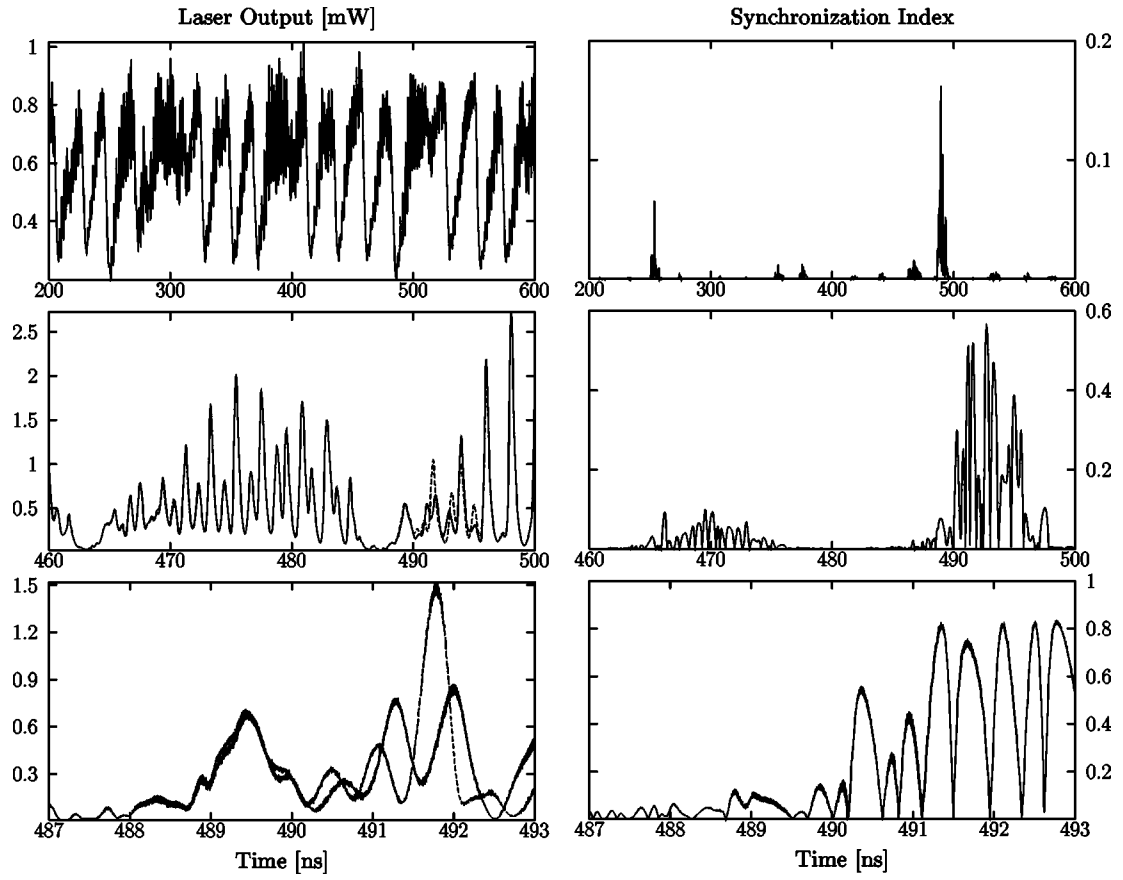

FIG. 9. Power (master in solid lines and slave in dashed) and synchronization index time series for the 20:80⇔80:20 case (see Fig. 4) at different time scales (starting from the top, filter or ''detector'' response times of 7.5 ns, 750 ps, and 75 ps).

plausible to understand this regime as a nonlinear amplification process [14,22].

We examined this case further by applying a 2 ns time shift to the slave output, which corresponds to the laser time separation. Figure 11 shows that there is a significant improvement in the synchronization quality, since the power dropout lag behavior disappears. Still, there are visible spikes in the SI graphs, but now during the power dropout recoveries, and they are narrower and smaller than those observed before during the power dropout event when the time shift was not included. The origin of these is the faster slave power recovery that occurs before the master injection is strong enough to bring both lasers back to synchronization. This is consistent with the nature of the synchronization observed, characterized as a nonlinear amplification process, which can be easily broken when the injection is weak enough.

For the asymmetric case 20:80⇔20:80 in Fig. 12, the feedback strength r_e^2 and injection strength t_e^2 were adjusted to 3.2% and 0.2%, and the slave output was properly scaled. In this case, the synchronization between the master and slave is the poorest one, and it does not improve very much when slower observational time scales are employed. Note, however, that the signals are still strongly coupled, since the master and slave power recoveries are synchronized, and the pulse structures are also essentially in phase, despite their different magnitudes. We observed this kind of synchronization, even in a symmetric system, when the coupling injection was weak compared to the feedback.

To investigate the origin of the strong loss of synchronization for the asymmetric cases, it is necessary to analyze the internal boundary conditions at the slave perturbed facet. Figure 13 shows the boundary conditions elements in the corresponding equation (14) for the original nonflipped configuration

$$E_s^+(t) = r_s E_s^-(t) + t_s t_e t_m E_m^+(t-\tau) = r_s E_s^-(t) + r_s \kappa_s E_m^+(t-\tau), \tag{14}$$

where κ_s is the LK coupling coefficient defined in Eq. (4). By analogy, if we write down the boundary condition for the flipped slave laser, we obtain

$$\hat{E}_s^+(t) = \hat{r}_s \hat{E}_s^-(t) + \hat{r}_s \hat{\kappa}_s E_m^+(t-\tau), \tag{15}$$

where $\hat{r}_s$ and $\hat{\kappa}_s$ are the new reflectivity and coupling coefficients in the perturbed facet after the flip, and $\hat{E}_S^+$ is the flipped field solution.

We can define the relative injection strength (RIS), denoted as R_{IS}, as the ratio between the terms in the slave boundary conditions in Eqs. (14) and (15),

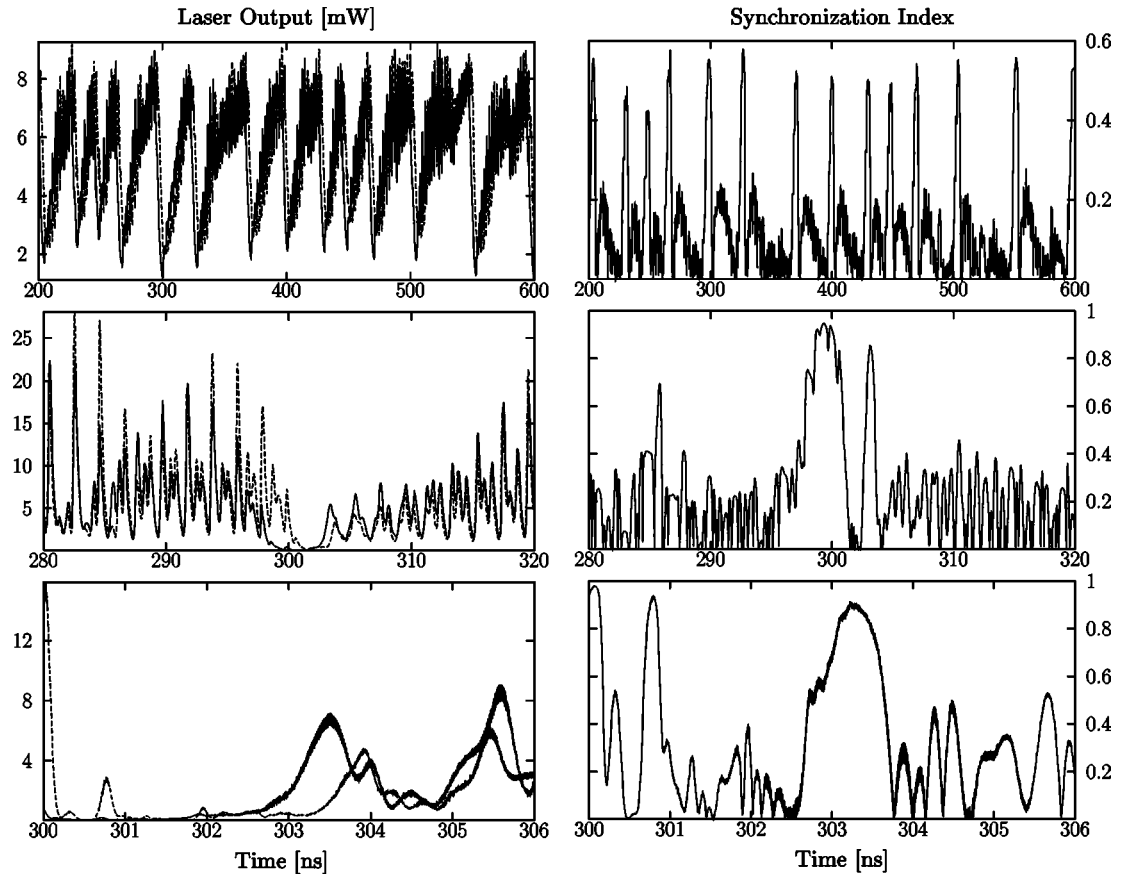

FIG. 10. Power (master in solid lines and slave in dashed) and synchronization index time series for the 80:20⇔80:20 case (see Fig. 4) at different time scales (starting from the top, filter or ''detector'' response times of 7.5 ns, 750 ps, and 75 ps).

$$R_{\mathrm{IS}}=\frac{r_s\kappa_s||E_m^+(t-\tau)||}{r_s||E_s^-(t)||}=\kappa_s\frac{||E_m^+(t-\tau)||}{||E_s^-(t)||},$$

$$\widehat{R_{\mathrm{IS}}}=\frac{\hat{r}_s\hat{\kappa}_s||E_m^+(t-\tau)||}{\hat{r}_s||\hat{E}_s^-(t)||}=\hat{\kappa}_s\frac{||E_m^+(t-\tau)||}{||\hat{E}_s^-(t)||}, \tag{16}$$

therefore

$$\widehat{R_{\mathrm{IS}}}=\frac{\hat{\kappa}_s}{\kappa_s}\frac{||E_s^-(t)||}{||\hat{E}_s^-(t)||}R_{\mathrm{IS}}. \tag{17}$$

It can also be shown (see the Appendix) that the relation between the nonflipped and flipped fields at the slave boundary condition is approximately given by

$$\frac{||E_s^-(t)||}{||\hat{E}_s^-(t)||}\approx\sqrt{\frac{\hat{r}_s}{r_s}}, \tag{18}$$

from where

$$\widehat{R_{\mathrm{IS}}}\approx\frac{\hat{\kappa}_s}{\kappa_s}\sqrt{\frac{\hat{r}_s}{r_s}}R_{\mathrm{IS}}. \tag{19}$$

If we preserve the LK coupling coefficients, then

$$\widehat{R_{\mathrm{IS}}}\approx\sqrt{\frac{\hat{r}_s}{r_s}}R_{\mathrm{IS}}. \tag{20}$$

This means that for the 80:20⇔80:20 case, the relative injection strength is approximately given by

$$\widehat{R_{\mathrm{IS}}}\approx\sqrt[4]{\frac{0.8}{0.2}}R_{\mathrm{IS}}=\sqrt{2}R_{\mathrm{IS}}. \tag{21}$$

Or in other words, for the 80:20⇔80:20 configuration the square of the flipped relative injection strength $\widehat{R_{\mathrm{IS}}}$ is about twice the original nonflipped one. Similarly, in the 20:80⇔20:80 case the square of the flipped relative injection strength $\widehat{R_{\mathrm{IS}}}$ is about half of the original nonflipped one. This is in line with the observation that the adjustment of the feedback strength r_e and injection strength t_e to keep a global LK coefficient, like we did with the four configurations before, was not the optimal choice for the asymmetric cases. In fact, in the 80:20⇔80:20 asymmetric case the resulting injection was too strong, producing the lag synchronization or nonlinear amplification regime, and in the 20:80⇔20:80 case, the resulting injection was too weak, producing a coupled but very poorly synchronized regime.

To verify that the loss of the relative injection strength was the main reason of the loss of synchronization, we proceed to vary the flipped injection factor $\hat{t}_e$ in order to main-

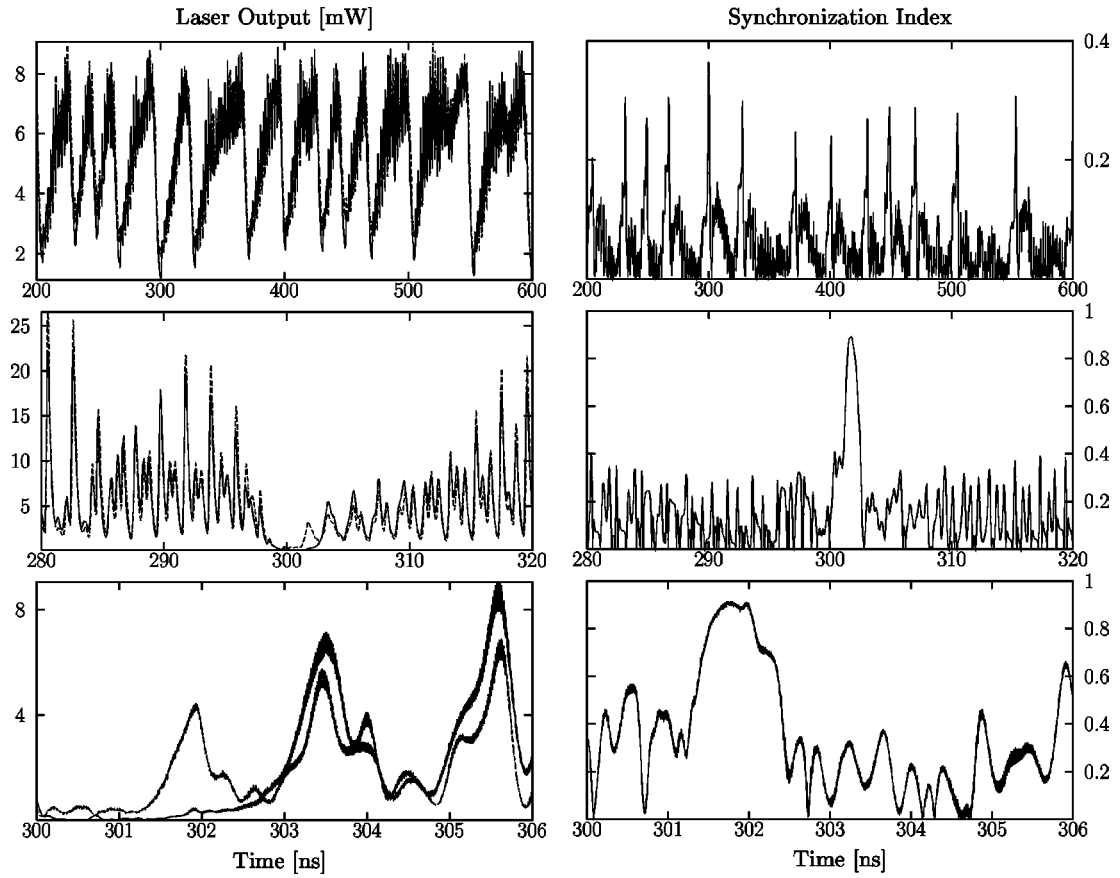

FIG. 11. Power (master in solid lines and slave in dashed) and synchronization index time series for the time shifted 80:20⇔80:20^s case at different time scales (from the top, filter or ''detector'' response times of 7.5 ns, 750 ps, and 75 ps).

tain the RIS ratio instead of the global LK coupling coefficient; i.e., from Eq. (19) we set the flipped coupling coefficient $\hat{t}_e$ such that

$$\frac{\widehat{R_{\mathrm{IS}}}}{R_{\mathrm{IS}}}=\frac{\hat{t}_e\hat{t}_s}{t_e t_s}\sqrt{\frac{r_s}{\hat{r}_s}}=1,$$

which implies

$$\hat{t}_e=t_e\frac{t_s}{\hat{t}_s}\sqrt{\frac{\hat{r}_s}{r_s}}. \tag{22}$$

Note that by using the injection factor defined in Eq. (22) instead of the one that preserves the global LK coupling coefficient (5), we are departing to a case outside of the ''LK invariant'' family, since the new LK coupling coefficient will be

$$\hat{\kappa}_s=\kappa_s\sqrt{\frac{r_s}{\hat{r}_s}}, \tag{23}$$

and therefore within the LK model, nonsynchronization or poor synchronization must be observed when the ratio $\sqrt{r_s/\hat{r}_s}$ differs from 1, as it happens when the laser by itself is asymmetric and its facet reflectivities are not equal.

To preserve the flipped relative injection strength $\widehat{R_{\mathrm{IS}}}$ in the 80:20⇔80:20 case, the flipped injection strength $\hat{t}_e^2$ had to be adjusted to around 1.6%, or half of the 3.2% value previously used. In fact, after modifying it, we found an optimum synchronization coupling value at 1.57%. Figure 14 shows the power and SI time series for this optimal case, and as can be seen, there is a significant improvement in the system synchronization, principally because the lag behavior disappeared. However, the resulting synchronization quality is still behind the corresponding 80:20⇔20:80 symmetric case.

To preserve $\widehat{R_{\mathrm{IS}}}$ in the 20:80⇔20:80 configuration, $\hat{t}_e^2$ had to be set around 0.4%, or twice the 0.2% value previously used. As before, we also found a near-optimum value of 0.404%. The resulting power and SI time series for the optimal coupling are shown in Fig. 15.

From these adjusted parameter results, it is clear that to reach optimal synchronization in the asymmetric cases, the boundary conditions must be kept equivalent between the symmetric and asymmetric cases by trying to maintain the same RIS ratio instead of the LK global coefficient. However, even when that correction is applied, the synchronization quality it is still worse than in the symmetric cases.

This is evident when we compare Fig. 7, which shows the internal laser profiles and the output spectra for the symmetric case 80:20⇔20:80, and Fig. 16, which does the same for the optimal asymmetric case 20:80⇔20:80*.

As we mentioned before, in the symmetric case there is a mirror-image effect between the internal fields and carrier

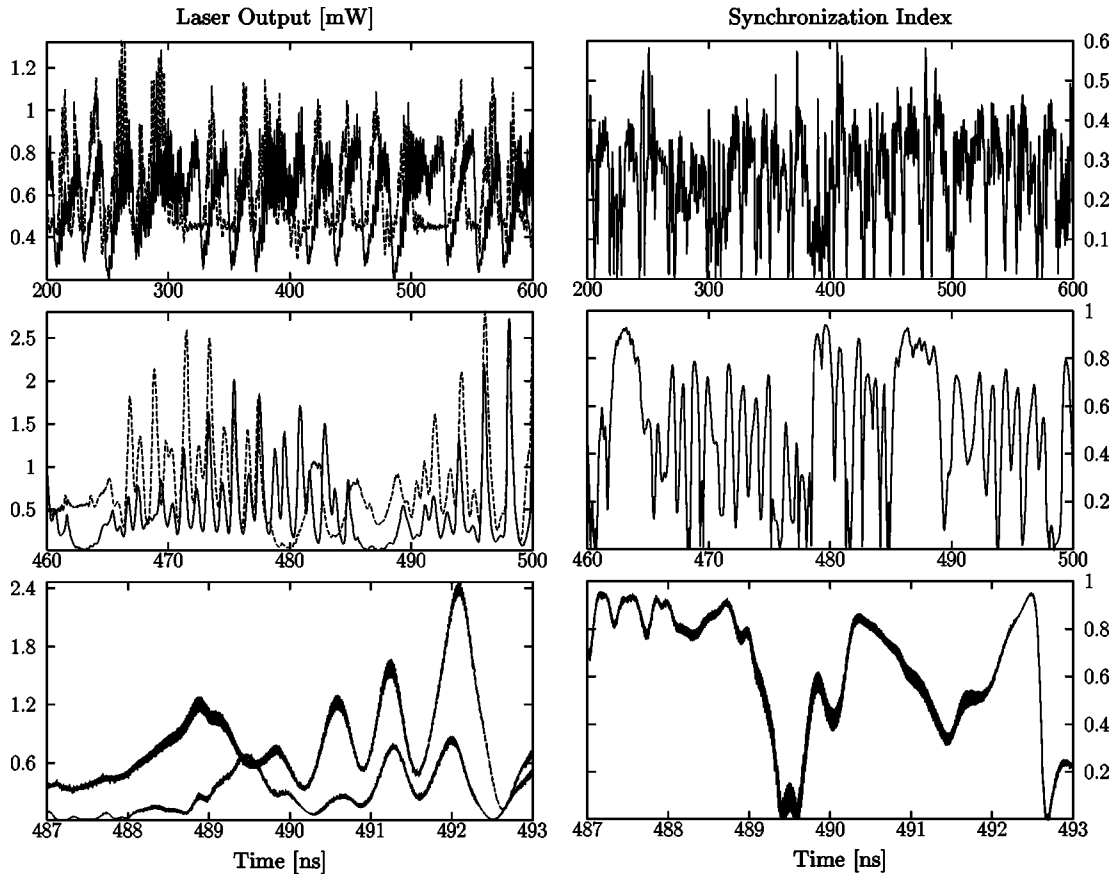

FIG. 12. Power (master in solid lines and slave in dashed) and synchronization index time series for the 20:80⇔20:80 case (see Fig. 4) at different time scales (starting from the top, filter or ''detector'' response times of 7.5 ns, 750 ps, and 75 ps).

density profiles when they reach complete or full synchronization. On the contrary, in the asymmetric case, even when the field profiles show some reflected similarity assuming proper scaling [compare the master forward fields (solid line) and slave backward fields (dashed lines) profiles, and vice versa], the carrier density profiles are clearly not showing the mirror-image effect. This is due to the asymmetry in the facet reflectivities, which imposes a marked orientation (especially for the carrier densities profiles) that cannot be reversed by the adjustment of the injection strength alone.

Moreover, given that the comparison of the corresponding internal field profiles and output powers must be done after proper scaling, the synchronization regime observed for the asymmetric configurations is a kind of ''localized synchronization'' [49,50], which means that the laser fluctuations are similar but they differ in amplitude. In fact, for the optimal asymmetric cases 20:80⇔20:80* and 80:20⇔80:20*, the output powers were remarkably different in amplitude, since the scaling factors b were around 6.4 and 0.18, respectively.

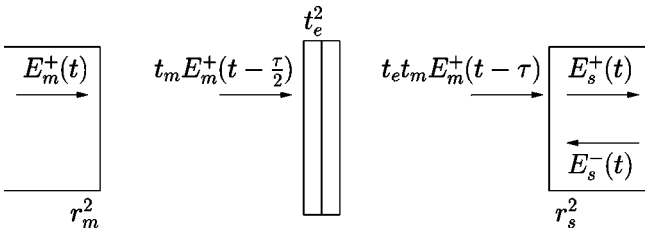

FIG. 13. Fields at the slave perturbed facet.

The marked carrier density profile orientation and the localized nature of the field synchronization prevent the system from reaching complete synchronization, since both lasers cannot yield near or identical solutions in the entire state variable space. This produces the observed loss of quality synchronization for the fastest time scales, and the discrepancies between the signal spectra. Note that the differences are more visible at both spectral resolutions, as they are computed by using the original nonaveraged raw complex field data that contain the amplitude and phase signal information.

To get a more global picture of the synchronization quality, we computed the power synchronization manifolds for the four configurations, considering the 2 ns time shift in the 80:20⇔80:20^s case, and the two optimal coupling injections found for both asymmetric cases. The manifolds were computed for the fast 75 ps and slow 7.5 ns observational time scales. The plots were constructed using the data over to the entire 1 μs simulation time window but undersampled since the number of data points exceeds the graphical resolution.

As it is shown in Fig. 17, at the 75 ps fast time scale the symmetric system 80:20⇔20:80 looks almost perfectly synchronized, with very small deviations from the diagonal. The second symmetric system 20:80⇔80:20 shows more obvious deviations from the diagonal for low power values, but still most of the sample data are contained in the synchro-

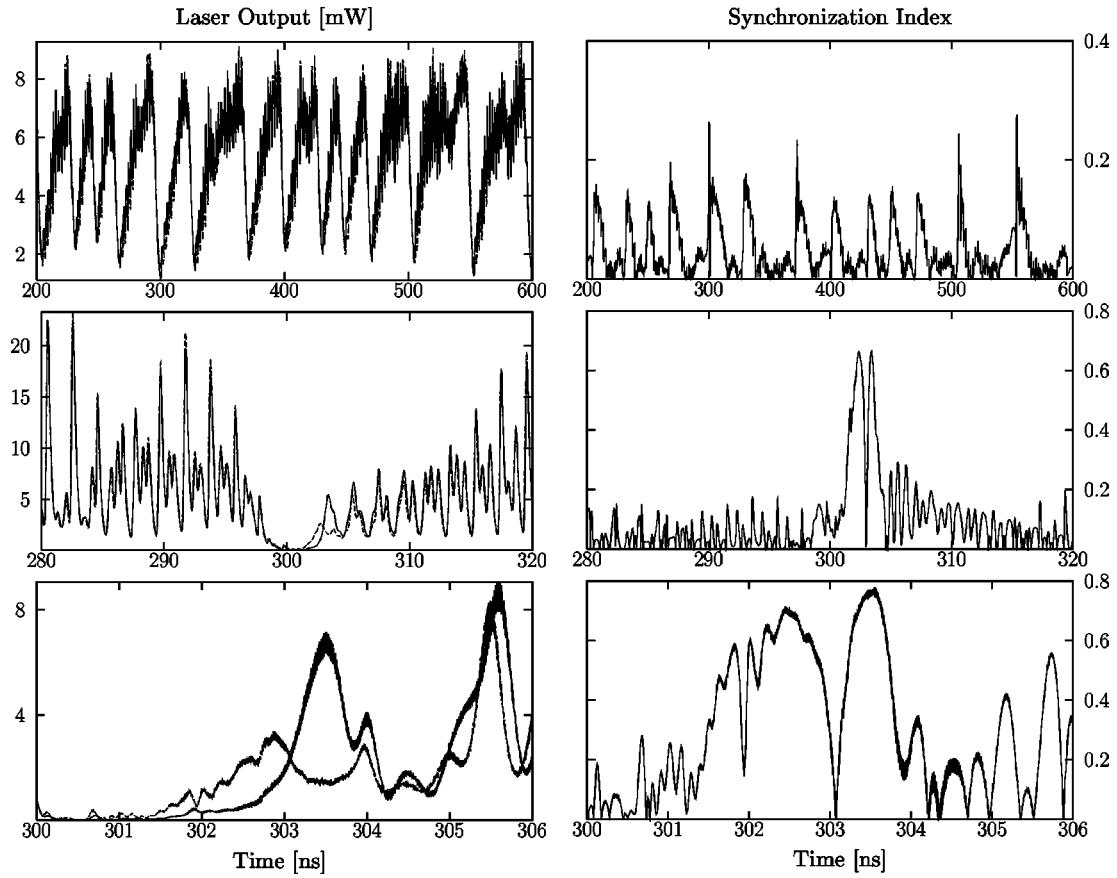

FIG. 14. Power (master in solid lines and slave in dashed) and synchronization index time series for the optimal 80:20⇔80:20* case at different time scales (starting from the top, filter or ''detector'' response of 7.5 ns, 750 ps, and 75 ps).

nized region. In the asymmetric 80:20⇔80:20^s time shifted configuration, the data pairs visibly spread outside the synchronized region, even when the 2 ns time shift is applied. For the optimal 80:20⇔80:20* case, the synchronization quality improves greatly, but it is never as good as the corresponding 80:20⇔20:80 symmetric case.

In the asymmetric system 20:80⇔20:80, the data pairs escape from the synchronized region and a horizontal feature appears. The latter is consistent with the prolonged power dropouts observed only in the slave laser (see Fig. 10). Here also the synchronization improves for the optimal 20:80⇔20:80* case obviously, but as before, the resulting quality is not as good as in the corresponding symmetric one.

At the 7.5 ns slow time scale in Fig. 18, like it was observed with the time series plots, the synchronization quality looks better and almost no deviations from the synchronized region appear in the symmetric systems. In the asymmetric time shifted 80:20⇔80:20^s and optimal 80:20⇔80:20* cases, the number of data pairs included in the synchronized region is much greater than that observed for the fast time scale, and now the synchronization for the optimal injections is much closer to that observed in the corresponding symmetric case.

For the 20:80⇔20:80 case, the horizontal feature that appears in the fast time scale picture is still visible, and most of the data pairs are also outside the synchronized region. For the optimal 20:80⇔20:80* case, on the other hand, there is a visible improvement in the synchronization quality, and it is also much closer to the symmetric one.

The power synchronization manifolds shown give us a picture of the global synchronization quality in the systems. In the graphs, however, two, ten, or hundred identical or very close data pairs will appear as one pair. So, even when the darker regions represent accumulation of data pairs, it is not possible to distinguish clearly between lightly and heavily populated regions.

With this in mind, we now introduce a global synchronization description based on the accumulated synchronization index histogram (ASIH) that in contrast to the power synchronization manifolds will give us a precise count of how many data points reside within or outside the synchronized region. The accumulated synchronization index histogram allows one to infer the degree to which the system remains synchronized over the entire simulation time window.

Figure 19 shows the ASIH for the different time scales used earlier (7.5 ns, 750 ps, and 75 ps), plus the 7.1-ps and the original 250-fs ones, corresponding to λ values of 10^{-1} and 1, respectively. In the pictures, for a given observational time scale or the corresponding filter response time FRT, one can read off the percentage of sampled data having a synchronization index equal to or less than some threshold. This percentage measures the global synchronization quality.

As we described before, the symmetric 80:20⇔20:80 case is the best synchronized, since the ASIH values for the

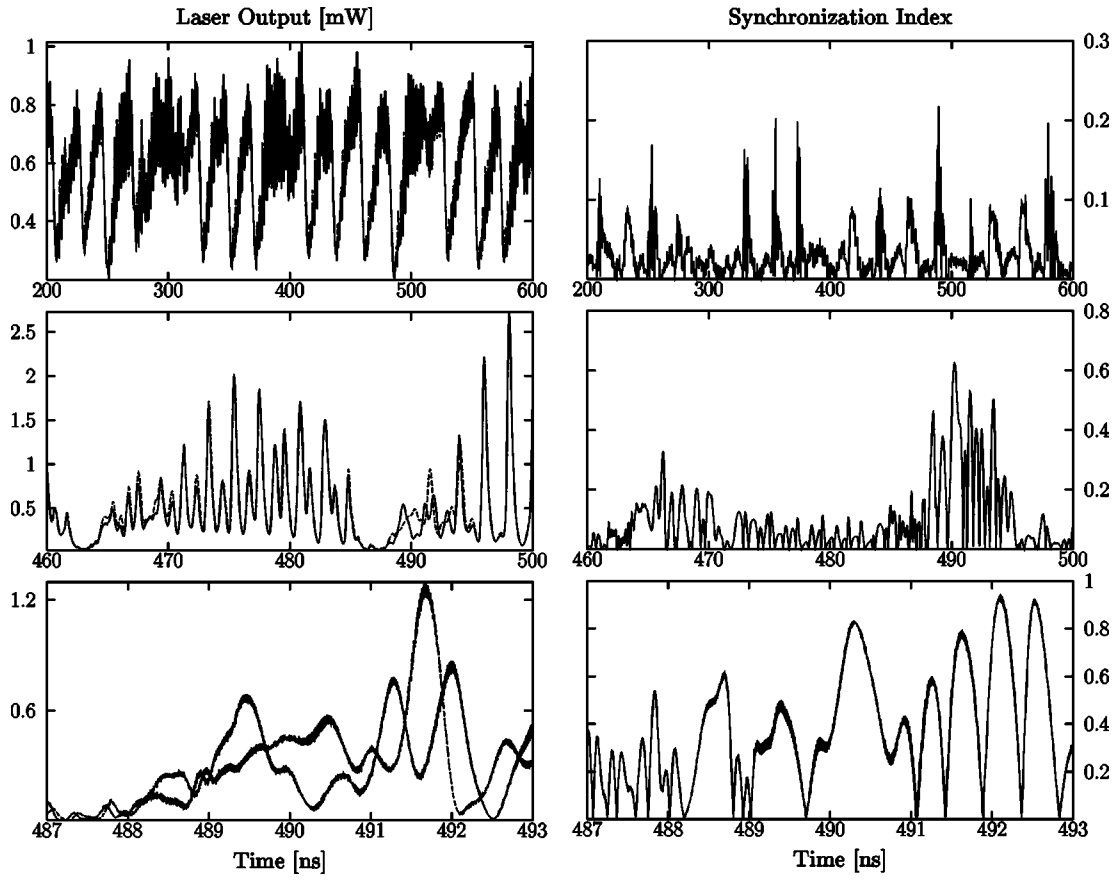

FIG. 15. Power (master in solid lines and slave in dashed) and synchronization index time series for the optimal 20:80⇔20:80* case at different time scales (starting from the top, filter or ''detector'' response times of 7.5 ns, 750 ps, and 75 ps).

chosen 0.2 SI threshold are equal to or greater than 99.9%, independent of the chosen time scale. This means that the power signals are almost perfectly synchronized for all the observational time scales and over the entire 1 μs simulation time window. For the symmetric 20:80⇔80:20 system, the lasers also show a very high degree of synchronization, where a very small degradation is observed for the fastest time scale, as the ASIH percentage slightly drops to a range between 98.7% and 99.9%.

In the asymmetric time shifted 80:20⇔80:20^s case, the loss of synchronization is visible for the LK coupling coefficient as the ASIH value drops to a range between 43.6% and 96.4%, even after applying the 2 ns time shift. When the optimal coupling is used instead, without any time shifting, the synchronization quality improves significantly and the ASIH value goes up to a range between 78.3% and 99.5%. For the asymmetric 20:80⇔20:80 configuration, the ASIH percentage for the LK coupling coefficient is in the range between 18.0% and 36.2%, showing a poorest synchronization quality. In fact, we can conclude that this system remains desynchronized for most of the simulation time window, independent of the observational time scale employed. This suggests us to name this regime as a ''locally coupled regime,'' capturing both the coupled and localized characteristics of its dynamics, but differentiating it from the other observed synchronized regimes. When the optimal coupling is used, the synchronization quality improves significantly and the ASIH percentage goes up to a range between 83.2% and 99.9%.

The asymmetric configurations show how the loss of symmetry makes the systems go from a very well-synchronized regime, where no major time scale dependence is observed, to the cases where the synchronization quality and its nature are changed. It is possible to go from a mainly desynchronized ''locally coupled regime,'' when the coupling coefficient is much smaller than the optimal one, to a ''localized lag synchronization,'' where the coupling coefficient is much larger than the optimal one. When the optimal coupling coefficients are employed, the laggard behavior disappears and very good ''localized synchronization'' can be observed, especially for the slow time scales. These show synchronization quality is comparable to the complete or full synchronization quality observed in the corresponding symmetric configurations. However, for the fastest time scales, the lag synchronization always shows a visible degradation with respect to the complete one.

Figure 20 summarizes the previous observations. It shows the accumulated synchronization index histogram value for the given 0.2-SI threshold as a function of the observational time scales or filter response times. The synchronization quality of the different discussed configurations can be analyzed through the corresponding curves in the picture.

As can be seen, the symmetric case 80:20⇔20:80 is the best synchronized one, with ASIH values of practically

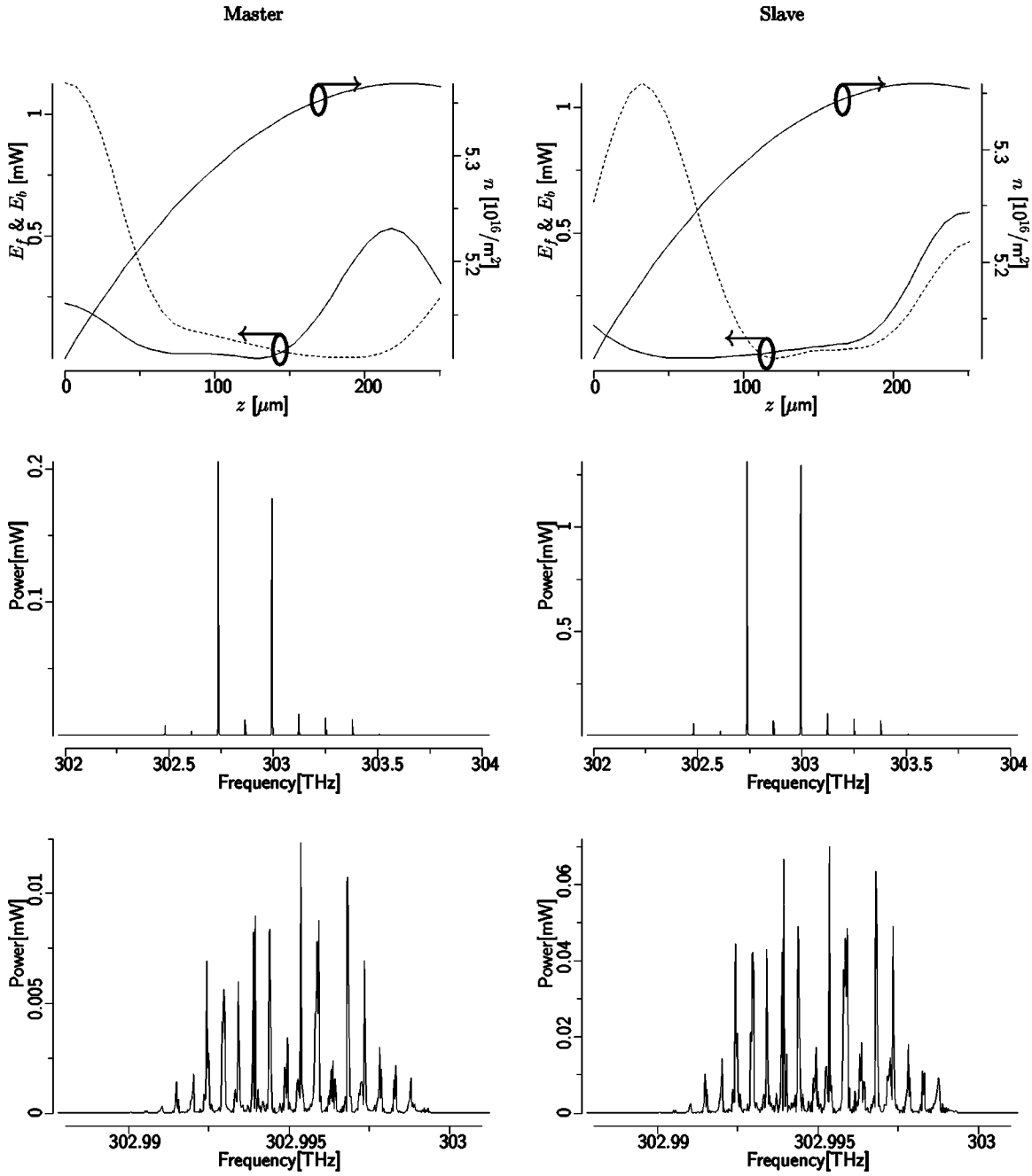

FIG. 16. Snapshot of the dynamics observed in the optimal 80:20⇔20:80* case. The top pictures show the internal fields (solid line for the forward field and dashed for the backward field) and carrier density profiles. The middle pictures show the multimode regime and the bottom ones show the broad chaotic signature in one of the frequency modes.

100% for all the filter response times computed. The second symmetric 20:80⇔80:20 case shows a slight loss of synchronization, since its ASIH percentage drops to 98.7% for the fastest time scale. The high synchronization quality for both cases is coming from the complete or full synchronization achieved in the whole state variable space, which allows to yield near to identical solutions in the master and slave lasers. The slight difference between both symmetric cases shows, however, that even two perfectly symmetric systems with identical laser devices can produce different synchronization dynamics. This requires further investigations as it can give some clues about what configurations are better suitable for synchronization purposes.

In the asymmetric case 80:20⇔80:20 under the LK global coupling coefficient, the synchronization quality drops dramatically especially for the fastest time scales. As was observed in the power time series, the main reason of this quality loss seems to be the laggard behavior observed in the slave laser, associated with the nonlinear amplification process that occurs when a much stronger relative injection is employed. Accordingly, the synchronization loss can be compensated by applying the 2 ns time shift, which corre-

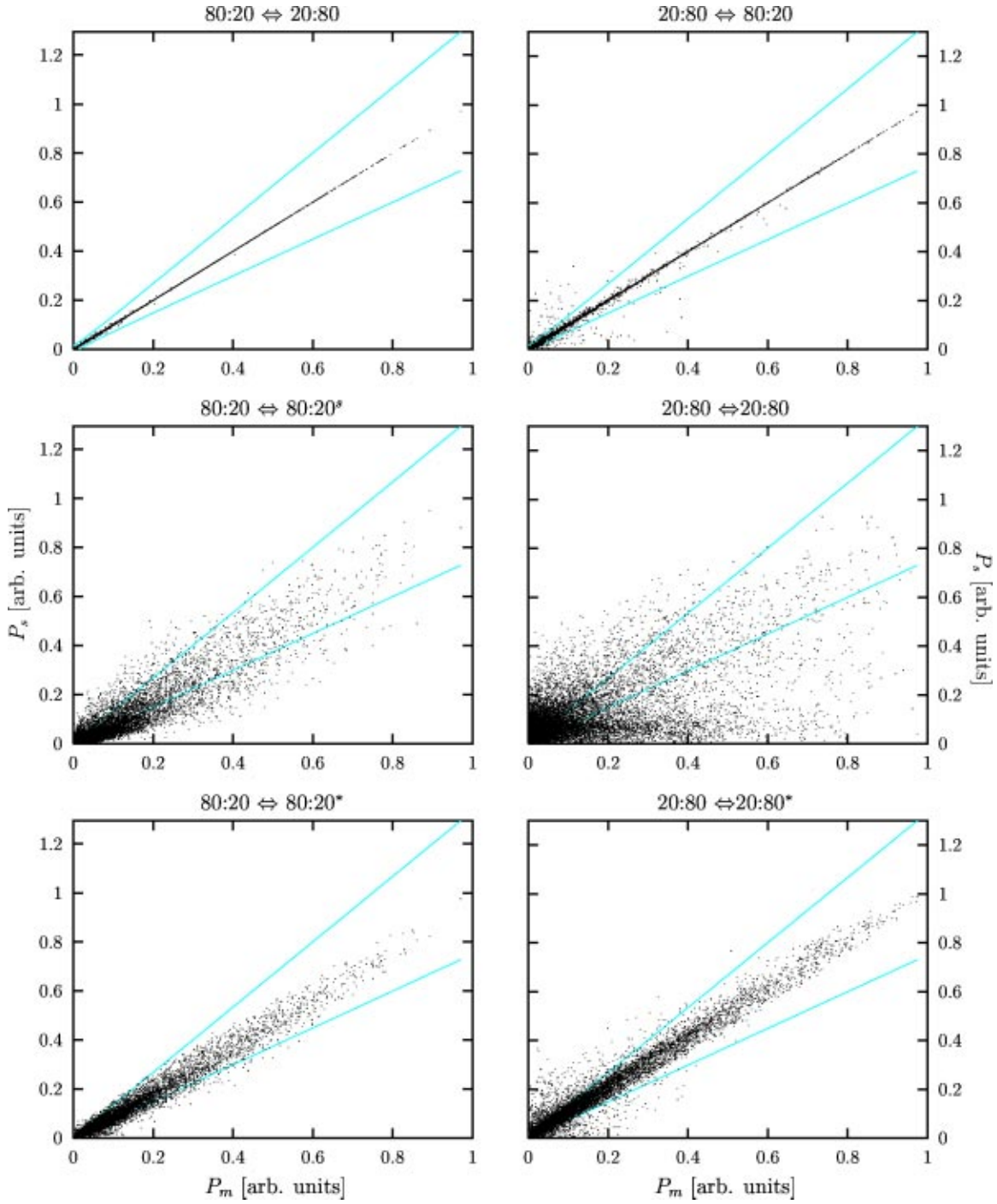

FIG. 17. Power synchronization manifolds for the 75 ps fast time scale. The first two pictures correspond to the symmetric cases; the two middle ones correspond to the asymmetric cases where the LK global coupling coefficient is preserved, and in the 80:20⇔80:20^s case a 2 ns time shift is included; and the last two lower pictures correspond to the asymmetric cases with optimal coupling coefficients. The solid lines represent the synchronized region limits.

sponds to the laser time separation, as it is shown in the 80:20⇔80:20^s curve. The improvements observed, however, are related to the slow characteristics of the signals, since they are smaller or hardly visible for the fastest time scales. When the optimal injection is employed, as can be seen for the 80:20⇔80:20* curve, the synchronization improves significantly, especially for the fastest time scales, since in the worst case the ASIH is around 20% below the corresponding value for the symmetric case 80:20⇔20:80.

For the asymmetric case 20:80⇔20:80, when the global LK coupling coefficient is maintained, the synchronization quality drops to levels where the system regime can no longer be considered as synchronized, but only as locally coupled. This is due to the resulting relative weak injection that is not strong enough to bring the slave laser into synchronization. For completeness, the 2 ns time shifted

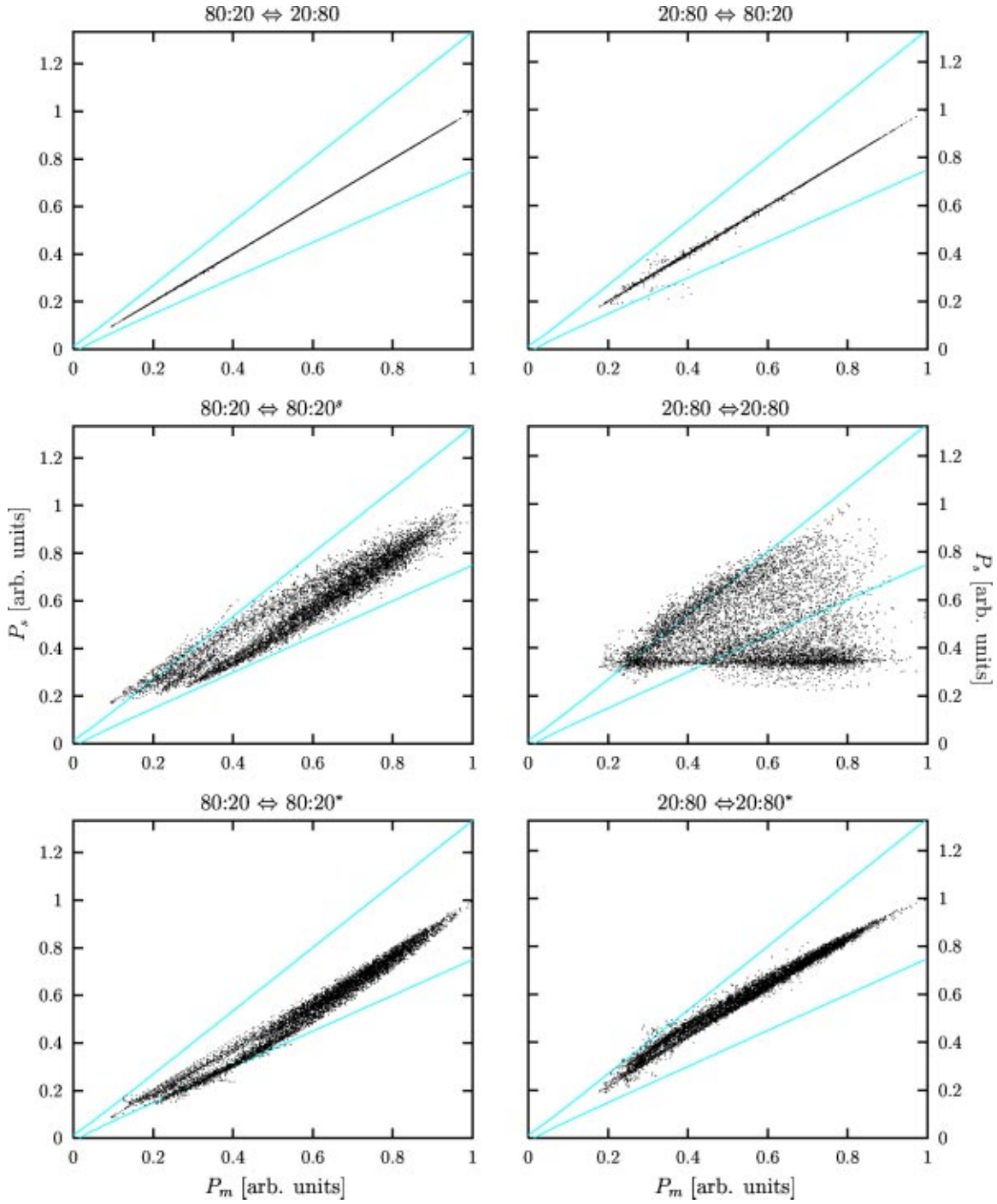

FIG. 18. Power synchronization manifolds for the 7.5 ns slow time scale. The first two pictures correspond to the symmetric cases; the two middle ones correspond to the asymmetric cases where the LK global coupling coefficient is preserved, and in the 80:20⇔80:20^s case a 2 ns time shift is included; and the last two lower pictures correspond to the asymmetric cases with optimal coupling coefficients. The solid lines represent the synchronized region limits.

20:80⇔20:80^s curve was also include in Fig. 20, but as it can be seen, the time shift applied only makes the synchronization quality slightly worse than the in-phase case. When the optimal injection coupling is employed, as is shown in the 20:80⇔20:80* curve, the synchronization quality for the slowest time scale is almost as good as that observed in the corresponding symmetric case, and for fastest time scale, it is also around 20% smaller.

For both the optimal asymmetric cases, the synchronization quality at the slowest time scales looks as good as in the symmetric cases, since the ASIH goes to values near to 100%. The loss of synchronization for the fastest time scales is produced by the remaining internal asymmetries, the marked hole space burning effects and the localized nature of the synchronization, which all prevent the system from reaching complete or full synchronization in the whole state

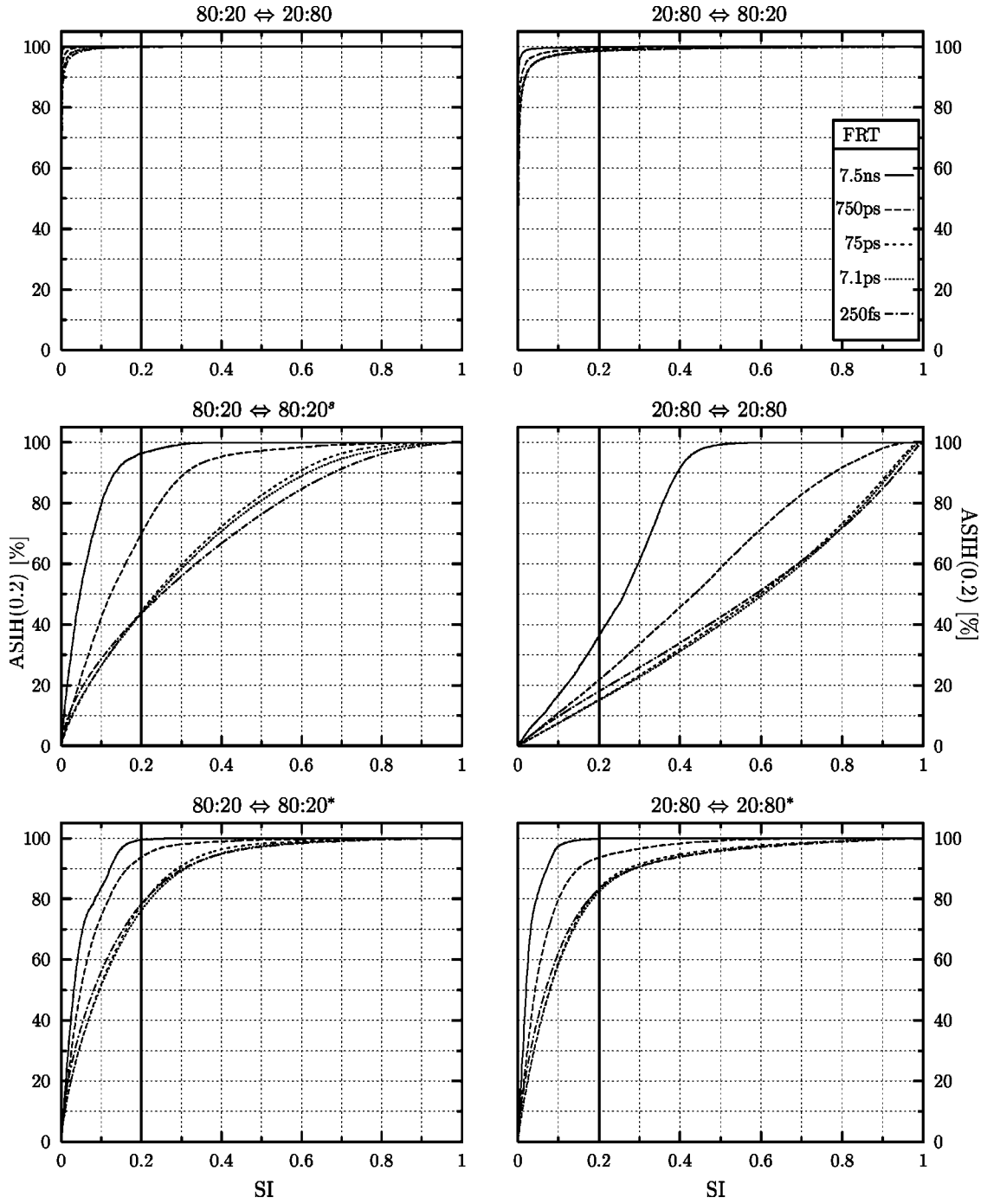

FIG. 19. Accumulated synchronization index histograms. The two top figures refer to symmetric cases; the middle ones to the asymmetric cases using the global LK coupling coefficient, where the $80{:}20 \Leftrightarrow 20{:}80^{s}$ includes the 2 ns time shift; and the last two are the asymmetric cases under optimal coupling conditions.

variable space. It should be noted that this inherent loss of synchronization, can be easily underestimated or not be seen at all when slow sensors or observational time scales are employed. This fact is particularly relevant for possible fast communications and encryption applications.

VII. CONCLUSIONS

We have presented simulation results of a full nonlinear partial differential equation semiconductor laser model where the optical material response is the input from gain/refractive index tables computed from a fully microscopic and experimentally validated theory. This allows us to quantitatively include the effects of frequency and carrier density dependent material susceptibilities, as well as proper boundary conditions.

The simulation model has been used to study realistic asymmetric extended Fabry-Perot laser devices, and the effects of their relative orientation on the quality of synchronization. In the analysis the studied system was a chaotic

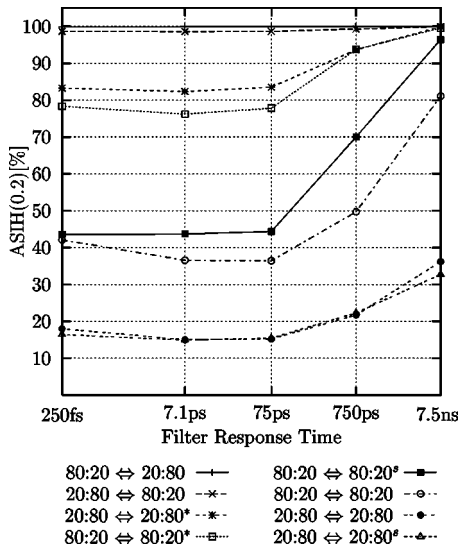

FIG. 20. ASIH values for the 0.2-SI threshold as a function of the filter or ''detector'' response times.

external cavity laser transmitter unidirectionally coupled to an originally nonchaotic laser receiver.

Details of the internal fields and boundary conditions are averaged out when the usual lumped-parameter Lang-Kobayashi model is employed. We have shown that very different laser configurations can be set up as a member of the same LK invariant family. The synchronization quality and its nature differ markedly for each of these different configurations despite the fact that each has an identical LK description. Sometimes, ''lucky snapshots'' of a poorly synchronized system can show apparent good synchronization, especially for slow observational time scales.

Our results show that by enforcing the LK equivalence, and contrary to what the LK model predicts, we encounter various types of synchronization behavior and regimes, including complete or full synchronization for the symmetric system, and localized lag synchronization and the desynchronized locally coupled regime for the asymmetric ones. This reveals the inherent LK model limitations related to the use of asymmetric devices and/or configurations.

The poor synchronization of asymmetrically oriented transmitter-receiver systems can be significantly improved by departing from the constraints associated with the single LK invariant family. By adjusting the feedback and injection strength close to the ones computed to keep the relative injection strength constant, optimal localized synchronization regimes can be found. However, even when the optimal parameters improve significantly the synchronization quality, it is never as good as in the symmetric cases. The persistent loss of synchronization in the asymmetric systems is due to strong spatial hole burning effects, the remaining system asymmetries, which cannot be compensated by the external adjustment of the injection strength alone, and the localized nature of the synchronization regime. All of these finally prevent the system from reaching complete or full synchronization in the whole state variable space.

We introduced SI and ASIH as more reliable measures of the synchronization quality locally and globally over long time intervals, respectively. We applied them to different observational time scales and showed that the observed synchronization quality not only depends strongly on the inherent properties of the analyzed system but also on the observational time scale or the detector response employed.

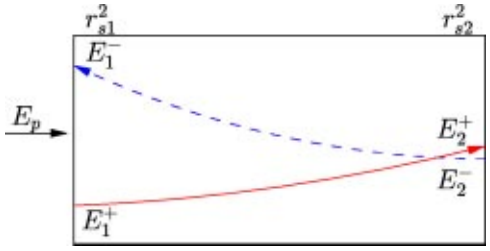

FIG. 21. Internal field diagram for the slave laser.

ACKNOWLEDGMENTS

The authors would like to thank C. Mirasso for many useful discussions. This work was supported by the U.S. Air Force Office of Scientific Research, the Air Force Material Command, USAF under Contract Nos. AFOSR-F49620-00-1-0002 and AFOSR-F49620-00-1-0190.

APPENDIX: RELATION BETWEEN THE NONFLIPPED AND FLIPPED BACKWARD FIELDS AT THE PERTURBED SLAVE FACET

Finding the approximate relation between the absolute backward field value $||E^-(t)||$ and the flipped one $||\hat{E}^-(t)||$ at the perturbed slave facet, as expressed in Eq. (17), is equivalent to find the relation between the maximum backward field E_1^- and the maximum forward field E_2^+ shown in Fig. 21.

Assuming that the laser is operating near the threshold value, in a steady state, and that the perturbation E_p is weak, then the forward and backward fields are amplified as follows:

$$E_2^+ \approx G E_1^+, \quad E_1^- \approx G E_2^-, \tag{A1}$$

and the respective boundary conditions for each facet impose the constraint

$$E_1^+ = r_{s1} E_1^-, \quad E_2^- = r_{s2} E_2^+. \tag{A2}$$

Combining Eqs. (A1) and (A2), we obtain

$$G \approx \frac{1}{\sqrt{r_{s1} r_{s2}}}, \quad E_1^- \approx \sqrt{\frac{r_{s2}}{r_{s1}}} E_2^+, \tag{A3}$$

thus, by renaming r_{s1} and r_{s2} as r_s, and $\hat{r}_s$, respectively,

$$\frac{||E_s^-(t)||}{||\hat{E}_s^-(t)||} \approx \frac{||E_1^-||}{||E_2^+||} \approx \sqrt{\frac{r_{s2}}{r_{s1}}} = \sqrt{\frac{\hat{r}_s}{r_s}}. \tag{A4}$$

[1] R. Lang and K. Kobayashi, IEEE J. Quantum Electron. **16**, 347 (1980).
[2] J. Mørk, B. Tromborg, and J. Mark, IEEE J. Quantum Electron. **28**, 93 (1992).
[3] R.W. Tkach and A.R. Chraplyvy, J. Lightwave Technol. **4**, 1655 (1986).
[4] A. Hohl and A. Gavrielides, Phys. Rev. Lett. **82**, 1148 (1999).
[5] I. Fischer, O. Hess, W. Elsäßer, and E. Göbel, Phys. Rev. Lett. **73**, 2188 (1994).
[6] R. Roy and K.S. Thornburg, Phys. Rev. Lett. **72**, 2009 (1994).
[7] T. Sugawara, M. Tachikawa, T. Tsukamoto, and T. Shimizu, Phys. Rev. Lett. **72**, 3502 (1994).
[8] Y. Takiguchi, H. Fujino, and J. Ohtsubo, Opt. Lett. **24**, 1570 (1999).
[9] S. Sivaprakasam and K.A. Shore, Opt. Lett. **24**, 466 (1999).
[10] D.Y. Tang, R. Dykstra, M.W. Hamilton, and N.R. Heckenberg, Chaos **8**, 697 (1998).
[11] S. Tang, H.F. Chen, and J.M. Liu, Opt. Lett. **26**, 1489 (2001).
[12] H. Fujino and J. Ohtsubo, Opt. Lett. **25**, 625 (2000).
[13] I. Wedekind and U. Parlitz, Int. J. Bifurcation Chaos Appl. Sci. Eng. **11**, 1141 (2001).
[14] I. Fischer, Y. Liu, and P. Davis, Phys. Rev. A **62**, 011801 (2000).
[15] A. Uchida, T. Ogawa, M. Shinozuka, and F. Kannari, Phys. Rev. E **62**, 1960 (2000).
[16] A. Uchida, Y. Liu, I. Fischer, P. Davis, and T. Aida, Phys. Rev. A **64**, 023801 (2001).
[17] G.D. VanWiggeren and R. Roy, Science **279**, 1198 (1998).
[18] S. Sivaprakasam and K.A. Shore, IEEE J. Quantum Electron. **36**, 35 (2000).
[19] J. Paul, S. Sivaprakasam, P.S. Spencer, R. Rees, and K.A. Shore, Electron. Lett. **38**, 28 (2002).
[20] J.K. White and J.V. Moloney, Phys. Rev. A **59**, 2422 (1999).
[21] V. Ahlers, U. Parlitz, and W. Lauterborn, Phys. Rev. E **58**, 7208 (1998).
[22] A. Murakami and J. Ohtsubo, Phys. Rev. A **65**, 033826 (2002).
[23] Y. Liu, H.F. Chen, J.M. Liu, P. Davis, and T. Aida, Phys. Rev. A **63**, 031802 (2001).
[24] I.V. Koryukin and P. Mandel, Phys. Rev. E **65**, 026201 (2002).
[25] F. Rogister, A. Locquet, D. Pieroux, M. Sciamanna, O. Deparis, P. Mégret, and M. Blondel, Opt. Lett. **26**, 1482 (2001).
[26] A. Locquet, C. Masoller, and C. Mirasso, Phys. Rev. E **65**, 056205 (2002).
[27] A. Locquet, C. Masoller, P. Mégret, and M. Blondel, Opt. Lett. **27**, 31 (2002).
[28] A. Locquet, F. Rogister, M. Sciamanna, P. Mégret, and M. Blondel, Phys. Rev. E **64**, 045203 (2001).
[29] V. Annovazzi-Lodi, S. Donati, and A. Scire, IEEE J. Quantum Electron. **33**, 1449 (1997).
[30] C.R. Mirasso, P. Colet, and P. García-Fernández, IEEE Photonics Technol. Lett. **8**, 299 (1996).
[31] A. Sánchez-Díaz, C.R. Mirasso, P. Colet, and P. García-Fernández, IEEE J. Quantum Electron. **35**, 292 (1999).
[32] S.F. Yu, P. Shum, and N.Q. Ngo, Opt. Commun. **200**, 143 (2001).
[33] P.S. Spencer, C.R. Mirasso, P. Colet, and K.A. Shore, IEEE J. Quantum Electron. **34**, 1673 (1998).
[34] J. Revuelta, C.R. Mirasso, P. Colet, and L. Pesquera, IEEE Photonics Technol. Lett. **14**, 1041 (2002).
[35] C.R. Mirasso, J. Mulet, and C. Masoller, IEEE Photonics Technol. Lett. **14**, 456 (2002).
[36] J. Mulet, C. R. Mirasso, T. Heil, and I. Fischer, in *Physics and Simulations of Optoelectronics Devices* (SPIE, San Jose, CA, 2001), pp. 293–302.
[37] T. Heil, I. Fischer, W. Elsäßer, J. Mulet, and C.R. Mirasso, Phys. Rev. Lett. **86**, 795 (2001).
[38] C.R. Mirasso, M. Kolesik, M. Matus, J.K. White, and J.V. Moloney, Phys. Rev. A **65**, 013805 (2002).
[39] M.G. Rosenblum, A.S. Pikovsky, and J. Kurths, Phys. Rev. Lett. **78**, 4193 (1996).
[40] J. Ohtsubo and H. Fujino, in *Proceedings of the 13th Annual Conference of Lasers and Electro-Optics Society 2000*, edited by A. Owyoung (IEEE, Rio Grande, PR, 2000), Vol. 2, pp. 732–733.
[41] V. Annovazzi-Lodi, S. Donati, and A. Scire, IEEE J. Quantum Electron. **32**, 953 (1996).
[42] H.D.I. Abarbanel, M.B. Kennel, L. Illing, S. Tang, H.F. Chen, and J.M. Liu, IEEE J. Quantum Electron. **37**, 1301 (2001).
[43] H.F. Chen and J.M. Liu, IEEE J. Quantum Electron. **36**, 27 (2000).
[44] L. Rahman, G. Li, and F. Tian, Opt. Commun. **138**, 91 (1997).
[45] A. Uchida, T. Ogawa, and F. Kannari, Jpn. J. Appl. Phys., Part 2 **37**, L730 (1998).
[46] J. Hader, J.V. Moloney, and S.W. Koch, IEEE J. Quantum Electron. **35**, 1878 (1999).
[47] M. Kolesik and J.V. Moloney, IEEE J. Quantum Electron. **37**, 936 (2001).
[48] N. Schunk and K. Petermann, IEEE J. Quantum Electron. **24**, 1242 (1988).
[49] R. Kuske and T. Erneux, Opt. Commun. **139**, 125 (1997).
[50] A. Hohl, A. Gavrielides, T. Erneux, and V. Kovanis, Phys. Rev. Lett. **78**, 4745 (1997).